Scientific and Technological Alliance for Guaranteeing the European Excellence in Concentrating Solar Thermal Energy

Deliverable D12.9

Final Report with Conclusions and Systems Identified

WP12 – Task 12.2	Deliverable D12.9
Due date:	January/2018
Submitted	January/2018
Partner responsible	US
Person responsible	Manuel Silva
Author(s):	Marcelino Sánchez, Amaia Mutuberria, Iñigo Les, Alain Ferriere, Miguel A. Reyes, Manuel Romero, José González-Aguilar, F. Javier Pino, Francisco Cabello, Elena Pérez, Manuel Silva
Document version:	1
Reviewed/supervised by:	
Dissemination Level	PU

List of content

Figures

Tables

Foreword

This is a technical report corresponding to the deliverable D12.9, *Final report with conclusions and systems identified,* elaborated to define the configurations and the technical specifications of the solar power plant considered in the frame of subtask 12.2.7, to describe the modelling of power plant components, to present the simulation results for design point conditions and annual performance of the proposed configurations and lastly to summarize the main conclusions drawn from this subtask.

1 Introduction

The main objective of work package 12 (WP12) is to advance in the technology for the next generation of Solar Thermal Electricity (STE) plants using point focus concentrators, especially in solar tower technology. The work carried out under WP12 is divided into two tasks. Task 12.1 is focused on the development of low cost heliostat fields by using small heliostats that could be manufactured, installed and commissioned for less than 100 €/m^2 and ad-hoc control and fast calibration systems. Task 12.2 is focused on the development of improved high concentration optical systems and enhanced receiver concepts to solve current issues and minimizing optical and thermal losses and costs.

The panorama in solar tower commercial deployment is currently dominated by the molten salt technology. Molten salt towers with two-tank thermal energy storage systems is considered a mature technology, although there is still a large potential for improvement.

However, the full exploitation of the central receiver technology potential for high efficiency requires increasing the HTF temperature above the current 560 – 570 ºC achievable with the current molten salt mixtures. One of the most obvious alternatives is to use air as HTF. Some developments in the frame of Task 12.2 have been oriented in this direction (design and testing of volumetric absorber prototypes, flat-plate pressurized air receiver).

Regarding the heliostat field, the trend in recent commercial solar tower projects is to use larger aperture heliostats (up to 180 m^2). However, the alternatives considered in Task 12.1 to develop low cost heliostat fields and thus increase competitiveness of solar towers have explored the opposite direction. Small size heliostats exhibit some characteristics with the potential to improve performance or reduce the cost of the heliostat field.

2 Objective of this document

According to the DoW, the objective of subtask 12.2.7 is to identify a representative high concentration optical system (HCOS) based on the results of the WP12 and to provide a detailed assessment of the representative HCOS previously defined, in terms of overall integration in a power plant.

This report covers the project deliverable D12.9, *Final Report with Conclusions and Systems Identified*. Section 3 of this document describes the proposed plant configurations, all of them based on the results of previous activities of this work package. Once these configurations have been analysed sections 4 to 7 describe the characteristics of the main components of the plant: solar field, solar receiver, thermal energy storage (TES) system and power block. Since to achieve the goals of this subtask it is necessary to assess the performance of the different plant configurations, partners involved in this subtask have developed a tool for this purpose; the main characteristics of this tool are described in section 8. The last sections of this document show the main simulation results and summarize the key conclusions drawn from this work.

3   High Concentration Optical System

The HCOS is based on the developments carried out in the frame of WP12, namely the heliostat concepts developed in the frame of Task 12.1 (subtask 12.1.2) and the receiver concepts developed in the frame of Task 12.2 (subtask 12.2.3). In addition, the simulation tools and the results of the simulations developed in WP12 will be used for the optimization and assessment of the defined HCOS.

The HCOS should also consider other developments of WP12, like the fast calibration procedures developed in subtask 12.1.4, the flux measurement systems defined in subtask 12.2.5 or the control strategies and algorithms developed in subtask 12.2.6, although their implementation is not addressed in this report.

Initially, four configurations were proposed, all of them considering a total receiver thermal output of 100 MW$_{th}$:

- A multi-tower configuration without thermal energy storage. The system consists of 20 units, each comprising a north field, one cavity receiver module of 5 MW$_{th}$ and one gas turbine. The turbines are installed inside the towers, at approximately the receiver level (Option A in Figure 1).

- A single tower, with surrounding field and multi-cavity receiver, connected to a hybrid (solar-gas) combined cycle (Brayton-Rankine). Three variants or options are considered:

    o Thermal Storage System (TES) fed by gas turbine exhaust and feeding the heat recovery steam generator (HRSG); the combustor is in series with the receiver output (Option B.1 in Figure 1).

    o TES fed by the receiver thermal output and feeding the gas turbine; a gas combustor is in series with the TES output to provide stability (Option B.2 in Figure 1).

    o No TES; the combustor is in series with the receiver output (Option B.3 in Figure 1).

After discussion of these alternatives, partners decided to drop option A since they considered that the possibilities of this proposal, in terms of solar industry implementation, are fewer than the opportunities linked to option B configurations. There are two main differences between configurations A and B. The first one is that configuration A employs a multi-tower system and north fields while each configuration of option B includes a single tower and a surrounding solar field. The second difference between options A and B is the thermodynamic cycle employed in each case, a Brayton cycle in option A and a combined cycle in option B. Partners did not consider that the use of the Brayton cycle provided added value compared with the combined cycle since the performance of the first one is around 40% while plants using combined cycles reach efficiencies up to 55%.
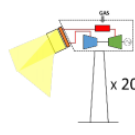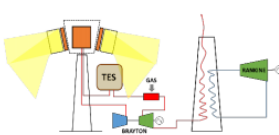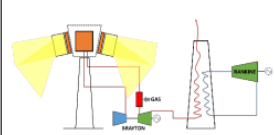
OPTION	A	B.1	B.2	B.3
NAME	MULTITOWER NO-STORAGE	SINGLE TOWER MULTI-CAVITY + TES (Turbine output)	SINGLE TOWER MULTI-CAVITY +TES (Turbine input)	SINGLE TOWER MULTI-CAVITY NO-STORAGE
SCHEME	x 20			
RECEIVER	PRESSURIZED AIR RECEIVER	PRESSURIZED AIR RECEIVER	PRESSURIZED AIR RECEIVER	PRESSURIZED AIR RECEIVER
NOMINAL POWER	5MWth	100 MWth (4x25MWth)	100 MWth (4x25MWth)	100 MWth (4x25MWth)
OPTICAL SYSTEM	CAVITY	CAVITY	CAVITY	CAVITY
SOLAR FIELD	NORTH FIELD	CIRCULAR FIELD	CIRCULAR FIELD	CIRCULAR FIELD
TERM. CYCLE	BRAYTON	COMBINED CYCLE	COMBINED CYCLE	COMBINED CYCLE
TURBINE	INSIDE THE TOWER	ON-GROUND	ON-GROUND	ON-GROUND
STORAGE	NO STORAGE	YES (GAS TURBINE OUTPUT)	YES (GAS TURBINE INPUT)	NO STORAGE
CLOUD TRANSIENTS	FUEL HYBRIDISATION	FUEL HYBRIDISATION	FUEL HYBRIDISATION & TES	FUEL HYBRIDISATION
COOLING	NOT NEED	DRY/WET COOLING	DRY/WET COOLING	DRY/WET COOLING

Figure 1. Power plant proposed layouts.

The detailed assessment of the HCOS is performed on a hypothetical STE plant with the following main characteristics:

- Overall plant concept according to the HCOS options B.1, B.2 and B.3 defined in Figure 1.
- Solar thermal power output: 100 MW$_{th}$.
- Plant gross output (MW$_e$): configuration dependent.
- Thermal energy storage capacity: 6 full-load equivalent hours, options B.1 and B.2.
- Alternative / auxiliary fuel: natural gas.
- Capacity factor and solar fraction: to be optimized for each option.
- Cost and financial data: The scenarios will be based on WP12 results where possible, or most updated public information available.

The location selected to place the solar power plant is Seville. For the purpose of this subtask, a flat site with no significant restrictions in terms of site boundaries will be considered. Table 1 summarizes geographical data and main calculation parameters.

Table 1. Geographical data and main calculation parameters.

Location	Seville (Spain)
Latitude	37.38º (N)
Longitude	-5.98º (W)
Altitude above sea level	7 meters
Design Direct Normal Irradiance (DNI)	950 W/m^2
Annual DNI	2050 kWh/m^2
Design time	21st December, noon

The selected design point for this study was the 21 December noon. This decision was taken because this is the time on which the power plant operation conditions are more restrictive from the equipment requirements point of view, which is directly linked to the durability of materials.

In the frame of this subtask a solar receiver design still under development has been employed, so design conditions on the receiver safe side have been chosen.

4 Solar field

The aim of the solar field optimization process is to define the layout that maximizes its annual average optical efficiency, calculated as the quotient between the energy impinging the receiver and the total energy available. A summary of the main input parameters and characteristics of the optimization tool are presented in subsections 4.1 and 4.2, while subsection 4.3 shows the obtained results.

4.1 Input parameters

As mentioned above, within subtask 12.1.2 of STAGE-STE project, a new concept of a single facet small heliostat has been studied. Based on this approach, five heliostats prototypes have been developed. The heliostat designed jointly by IK4-TEKNIKER and CENER has been selected for the HCOS. The main features of this heliostat model are presented in Table 2.

Table 2. Heliostat specifications.

Shape and dimensions	
Shape	Spherical rectangle
Width	3.21 m
Height	2.20 m
Curvature Radius	Two times the slant range
Pedestal height	0 m, the ground is considered a perfect plane
Optical properties	
Reflectivity	93.5 – 95 % Clean / 90 % Average
Optical error	2 mrad
Tracking system	
Tracking error	1 mrad
Tracking mode	Azimuth-Elevation

Table 3 summarizes the relevant parameters, assumptions, conditions and input data used for the solar field optimization process. As the last line of this table shows throughout this work it has been considered that the four receiver modules are identical. From a technical point of view this is motivated because the receiver considered in this study is still at the experimental stage, so an attempt has been made to protect the receiver design and try to impose that the four receiver modules work under controlled conditions ($30.3 MW_{th}$).

Table 3. Input parameters.

Location (Seville, Spain)	
Latitude	37.38º
Longitude	-5.98º
Annual DNI	2050 kWh/m^2. The same TMY file used in the reference plant proposed for evaluating the WP12 KPIs.

Atmospheric attenuation model	
DELSOL3 clear day [1]	

Tower	
Dimensions	Rectangular parallelepiped (17.6 x 17.6 x 108.652) m
Base center coordinates	(0, 0, 0)

Receiver (specifications of each one of the four individual receivers)	
Shape	Rectangle
Aperture Width	5 m
Aperture Height	5 m
Aperture Tilt angle	16.4º with respect to the vertical
Receiver centre/aiming point	North field (0, 100, -9.636) South field (0, 100, 9.636) East field (9.636, 100, 0) West field (-9.636, 100, 0)
Absortance	100%

Design Point	
Sun Position	21st December, noon, (180.016º azimuth and 60.8288º zenith)
DNI	950 W/m^2
Required power	121.2 MWth (4 x 30.3 MWth)

4.2 Solar field optimization

The optimization of the solar field is based on the use of the Solar Power Tower Integrated Layout and Optimization Tool (SolarPILOT) [2] that generates and characterizes power tower systems. This software was developed by the National Renewable Energy Laboratory (NREL). SolarPILOT consists of a graphical user interface (GUI) and an application programming interface (API) through which external programs can access SolarPILOT's functionality. SolarPILOT's calculation engine extends Sandia National Laboratories' DELSOL3 by using the computationally efficient Hermite expansion technique; it applies calculations to each heliostat image, rather than to larger groups of heliostats - as DELSOL3 does. SolarPILOT generates a heliostat field layout through the following multi-step process:

- Potential heliostat positions are identified, according to the selected layout method, within the feasible land area.

- SolarPILOT simulates the performance of all potential heliostat positions over the set of all point simulations: information on the performance of each heliostat is accumulated over all simulations. Each simulation is independent of the others in the set and may incorporate instantaneous or average weather data, as specified by the user. All significant optical effects are considered in the simulation, including cosine losses, heliostat reflectivity, blocking and shading, atmospheric attenuation, intercept factor and receiver surface reflectivity.

- All potential heliostats are ordered according to the accumulated performance (greater to lower) of all simulations. In our case, an annual simulation has been selected and the optical efficiency is the variable to be optimized (maximized).

- SolarPILOT executes a single reference point simulation for the design values conditions, and the total power delivered by each potential heliostat position is recorded.

- SolarPILOT proceeds through the sorted list of heliostats accumulating the power delivered by each one until the reference *Solar Field Design Power* is satisfied. If there are excess heliostats, they are deleted from the field layout. The remaining set of heliostats is the final heliostat field.

The optimization process described above is very close to the methodology proposed in subtask 12.1.5 of STAGE-STE where the evaluation of the optical efficiency is done for a typical meteorological year (TMY) taking into account all the optical losses.

4.3   Solar field optimization results

Solar field optimization begins with a solar field layout free optimization. It has been considered that the solar field is split into four fields, each of them aiming to a solar receiver module. Figure 2 shows the results of the initial optimization. Observe that there is some overlapping between the heliostat fields.
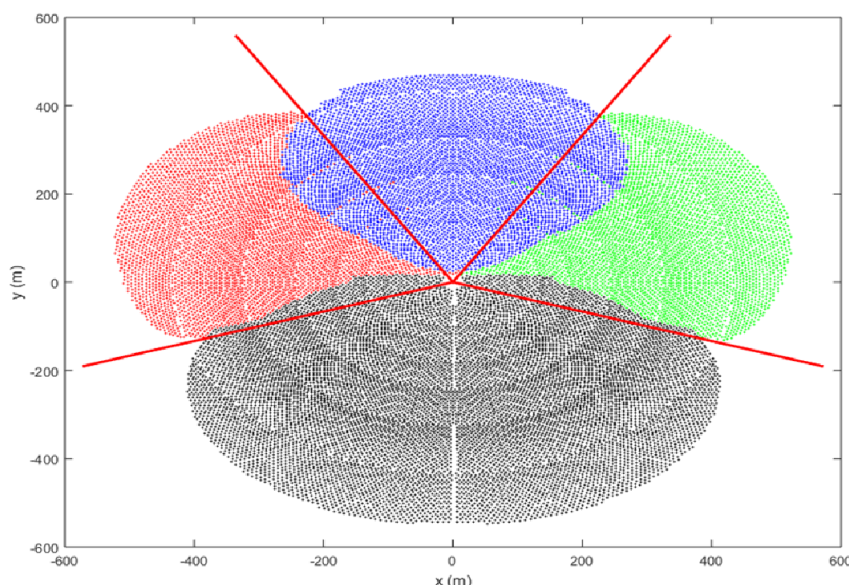
Figure 2. North, South, East and West fields after a free optimization.

From these results, a sensitivity analysis is performed to obtain the optimized angles covered by each solar field. Table 4 shows these results.

Table 4. Solar field angles.

Field	Angle
North	63º symmetric to the N-S axis
South	144º symmetric to the N-S axis
East	76.5º
West	76.5º

The selected method for the heliostat distribution is *Radial Stagger*. Once the optimized angles for each solar field are known, other influential parameters of this method are analyzed. Potential heliostat positions are distributed in circumference arcs whose center is determined by the position of the tower. A solar field that follows this distribution is characterized by the azimuthal separation between heliostats of a row and the radial separation between rows. These factors can be calculated from *Azimuthal Spacing Factor, Azimuthal Spacing Reset Limit* and *Packing Transition Limit Factor*. Table 5 summarizes optimized parameters for each solar field:

Table 5. Radial Stagger configuration parameters.

	North	South	East	West
Azimuthal Spacing Factor	2.0	1.3	1.8	1.8
Azimuthal Spacing Reset Limit	1.2	1.3	1.2	1.2
Packing Transition Limit Factor	1.1	1.1	1.1	1.1

The optimization progress finished successfully obtaining the solar field layout shown in Figure 3. A corridor 10 meters wide between heliostat fields is easily recognized.
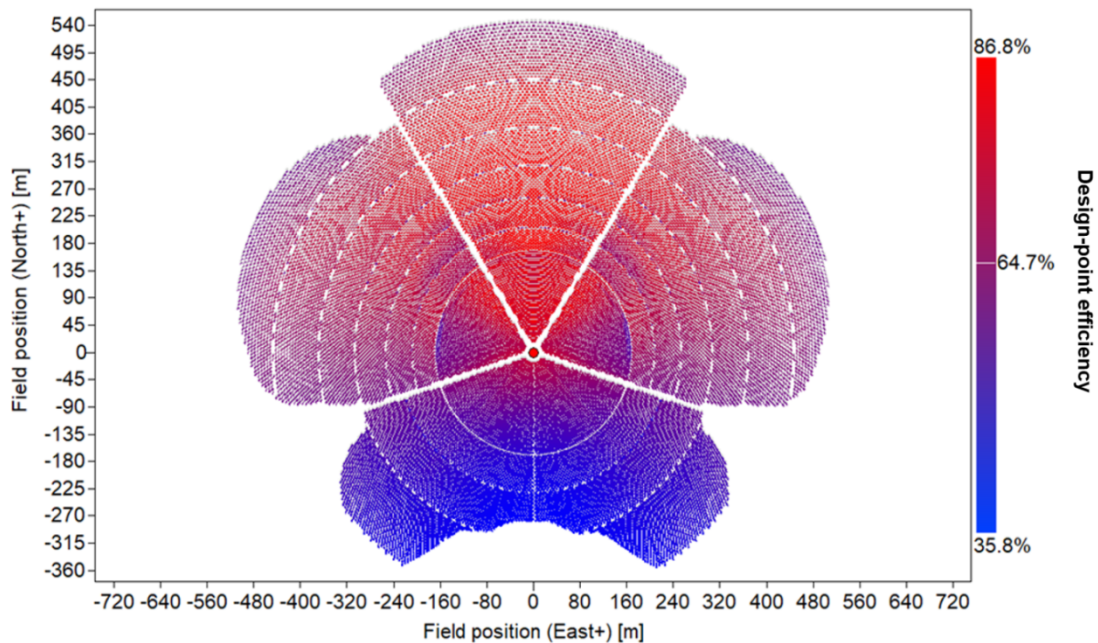
Figure 3. Annual efficiency of the optimized field.

Main characteristics of each solar field are shown in Table 6.

Table 6. Main characteristics and performance of the optimized solar field.

	North	South	East	West	All field
Number of heliostats	5658	9364	6505	6505	28032
Mirror area [m²]	39956.8	66128.6	45938.3	45938.3	197962.0
Power at design point [MWth]	30.33	30.28	30.24	30.24	121.1
Annual performance					
Total efficiency	0.6803	0.5398	0.6239	0.6202	0.6063
Cosine efficiency	0.8570	0.7134	0.7999	0.7875	0.7797
Shading efficiency	0.9451	0.9302	0.9413	0.9471	0.9397
Reflection efficiency	0.9000	0.9000	0.9000	0.9000	0.9000
Blocking efficiency	0.9971	0.9583	0.9866	0.9868	0.9793
Atmospheric attenuation	0.9610	0.9670	0.9620	0.9620	0.9635
Intercept efficiency	0.9715	0.9834	0.9760	0.9758	0.9775

* Total efficiency is not exactly the product of all other factors due to rounding

Table 7 to 11 show the efficiency matrices resulting from the optimization process.

Table 7. Efficiency matrix of the North field.

Azmimuth angles	Elevation angles						
	0.05°	5°	15°	25°	45°	65°	89.5°
50°	0.016	0.177	0.394	0.468	0.554	0.623	0.695
70°	0.018	0.165	0.459	0.543	0.608	0.652	0.695
90°	0.020	0.163	0.527	0.615	0.665	0.684	0.696
105°	0.021	0.143	0.547	0.661	0.704	0.707	0.696
120°	0.015	0.121	0.560	0.699	0.738	0.728	0.697
150°	0.018	0.093	0.592	0.753	0.786	0.758	0.697
180°	0.020	0.101	0.632	0.773	0.803	0.770	0.698
210°	0.018	0.093	0.592	0.753	0.786	0.758	0.697
240°	0.015	0.121	0.560	0.699	0.738	0.728	0.697
255°	0.021	0.143	0.547	0.661	0.704	0.707	0.696
270°	0.020	0.163	0.527	0.615	0.665	0.684	0.696
290°	0.018	0.165	0.459	0.543	0.608	0.652	0.695
310°	0.016	0.177	0.394	0.468	0.554	0.623	0.695

Table 8. Efficiency matrix of the South field.

Azmimuth angles	Elevation angles						
	0.05º	5º	15º	25º	45º	65º	89.5º
50º	0.012	0.020	0.419	0.588	0.681	0.674	0.653
70º	0.007	0.032	0.415	0.573	0.661	0.665	0.652
90º	0.007	0.040	0.405	0.550	0.637	0.653	0.652
105º	0.007	0.049	0.393	0.525	0.617	0.643	0.652
120º	0.008	0.059	0.374	0.499	0.597	0.633	0.652
150º	0.010	0.078	0.348	0.464	0.566	0.620	0.652
180º	0.011	0.092	0.361	0.456	0.554	0.617	0.652
210º	0.010	0.078	0.350	0.465	0.567	0.620	0.652
240º	0.008	0.058	0.376	0.501	0.598	0.633	0.652
255º	0.007	0.047	0.394	0.527	0.618	0.643	0.652
270º	0.007	0.039	0.406	0.551	0.638	0.653	0.652
290º	0.007	0.031	0.416	0.574	0.662	0.665	0.653
310º	0.012	0.020	0.419	0.588	0.681	0.674	0.653

Table 9. Efficiency matrix of the East field.

Azmimuth angles	Elevation angles						
	0.05º	5º	15º	25º	45º	65º	89.5º
50º	0.010	0.140	0.300	0.385	0.502	0.599	0.691
70º	0.010	0.144	0.283	0.371	0.492	0.594	0.691
90º	0.010	0.139	0.303	0.390	0.506	0.600	0.691
105º	0.011	0.147	0.347	0.429	0.531	0.611	0.691
120º	0.013	0.146	0.394	0.479	0.564	0.628	0.691
150º	0.015	0.118	0.481	0.587	0.643	0.669	0.692
180º	0.017	0.082	0.524	0.670	0.716	0.711	0.693
210º	0.016	0.059	0.558	0.724	0.768	0.744	0.694
240º	0.016	0.047	0.577	0.746	0.791	0.760	0.694
255º	0.017	0.048	0.583	0.748	0.792	0.761	0.694
270º	0.015	0.048	0.567	0.742	0.787	0.757	0.694
290º	0.016	0.061	0.559	0.723	0.767	0.744	0.694
310º	0.013	0.075	0.534	0.688	0.734	0.724	0.693

Table 10. Efficiency matrix of the West field.

Azmimuth angles	Elevation angles						
	0.05º	5º	15º	25º	45º	65º	89.5º
50º	0.013	0.075	0.534	0.687	0.733	0.723	0.693
70º	0.016	0.061	0.559	0.722	0.767	0.744	0.693
90º	0.015	0.048	0.567	0.742	0.786	0.756	0.694
105º	0.016	0.048	0.582	0.747	0.792	0.760	0.694
120º	0.016	0.047	0.577	0.746	0.791	0.759	0.694
150º	0.016	0.059	0.558	0.723	0.767	0.744	0.693
180º	0.017	0.082	0.524	0.670	0.716	0.711	0.693
210º	0.015	0.118	0.481	0.587	0.643	0.669	0.692
240º	0.013	0.147	0.395	0.479	0.564	0.628	0.691
255º	0.011	0.147	0.348	0.429	0.531	0.611	0.691
270º	0.010	0.139	0.303	0.390	0.506	0.600	0.690
290º	0.009	0.144	0.283	0.371	0.491	0.593	0.690
310º	0.010	0.139	0.300	0.385	0.502	0.598	0.690

Table 11. Efficiency matrix of the global field.

Azmimuth angles	Elevation angles						
	0.05º	5º	15º	25º	45º	65º	89.5º
50º	0.013	0.092	0.413	0.540	0.626	0.658	0.680
70º	0.012	0.092	0.427	0.555	0.636	0.664	0.679
90º	0.012	0.090	0.444	0.571	0.647	0.671	0.680
105º	0.013	0.091	0.457	0.582	0.655	0.676	0.680
120º	0.012	0.089	0.463	0.592	0.663	0.680	0.680
150º	0.014	0.086	0.477	0.611	0.675	0.688	0.680
180º	0.016	0.089	0.491	0.619	0.679	0.692	0.680
210º	0.014	0.086	0.478	0.612	0.676	0.688	0.680
240º	0.012	0.089	0.464	0.593	0.663	0.681	0.680
255º	0.013	0.090	0.458	0.583	0.656	0.676	0.680
270º	0.012	0.089	0.444	0.571	0.647	0.671	0.679
290º	0.012	0.091	0.427	0.555	0.636	0.664	0.680
310º	0.013	0.092	0.413	0.540	0.626	0.658	0.679

5 Solar receiver

The solar receiver is a key component of any solar tower system. It must fulfil many different requirements: high radiation-to-heat conversion efficiency, reliability, easy maintenance, long lifetime and low cost. The design, construction, implementation and operation of the solar receiver are strongly related to the design of the solar power plant and to the composition, temperature and pressure of the heat transfer fluid. Two different receiver module concepts have been proposed and assessed in the frame of subtask 12.2.3:

- A high temperature plate pressurized air receiver module.

- A molten salt receiver module with integrated storage.

Partners agreed to use the pressurized air receiver module concept because a more detailed assessment of this module, including experimental test results, was available. The design of this receiver is based on the technology developed by CNRS within the frame of the PEGASE project (Production of Electricity with Gas turbine and Solar Energy). The experience gained by CNRS through previous and current research works on the receiver technology [3][4][5] feeds into the collaborative WP12 of STAGE-STE project.

As Figure 1 shows, this subtask considers three plant configurations, but this does not impact the design of the receiver. In all configurations, the solar field is of the surrounding type. Therefore, the solar receiver must accommodate the omnidirectional solar radiation input. The overall 100 MW_{th} receiver is composed of four individual and identical receiver modules of 25 MW_{th} each. The apertures of these individual receiver modules are oriented towards four directions in the solar field: North, South, East and West. In the initial and simplified approach of the considered solar receiver, it is assumed that the four receiver modules are identical. Therefore, the design is made for one receiver module. Each one of the four individual receivers is made of a flat solar absorber and a cavity. The basic design of both components is presented in this section. The selected technology of flat plate absorbers utilizes copper/superalloy compound. For this technology, a receiver efficiency of 82.5% is predicted, along with 300 mbar pressure drop. Experimental testing has been carried out with a 30 kW prototype receiver in a test-bench under realistic operating conditions: concentrated solar energy and pressurized air with controlled flux density, inlet temperature and working pressure respectively. Outlet air temperature of 800°C was achieved under a flux of 600kW/m^2 at design air mass flow rate.

5.1 Solar absorber

The power transmitted to the fluid is 25 MW_{th}. The total area of the absorber is determined by the temperature gap between the fluid and the wall and the average heat transfer coefficient. Based on the performance assessed in previous works [5], CNRS assumed that the values of these parameters are 100 K and 1500 W/m^2·K respectively. In these conditions, the area of the absorber is 166.7 m^2. A square solar absorber is preferred. Associated to a square aperture of the cavity, this simple shape allows utilizing flat sheets of metal for the fabrication of the cavity. Finally, a square absorber of 12.9 m x 12.9 m is selected.

<u>Absorber modules</u>

The solar absorber is modular. The modular approach is motivated by the large size of the absorber and by the flexible arrangement which is necessary to comply with the multistage concept. Square absorber modules are selected. Each module features a bundle of tubes made of Ni-based alloy (Inconel 600®) embedded in a copper matrix. An external 2 mm foil of Ni-based alloy covers the cooper matrix and prevents oxidation. The resulting concept is a flat plate absorber. The internal tubes of 8 mm in diameter are set parallel to the main absorber surface. They are evenly spaced every 13 mm and arranged in five rows in the horizontal direction. The vertical distance between two adjacent rows is 15 mm. The resulting overall thickness of the receiver plate is typically 8 cm. A cross-section of this concept is represented in Figure 4.
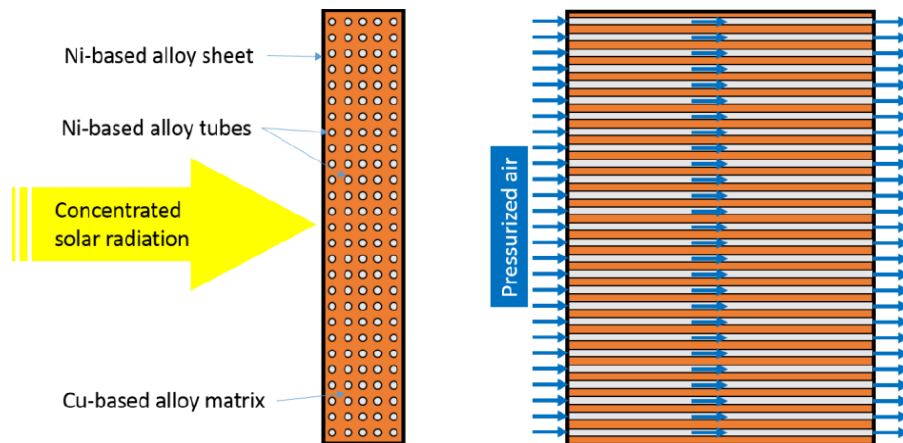

Figure 4. The concept of solar absorber module (patented by CNRS/CEA).

Twisted tapes are inserted into the small tubes to increase turbulence in the air flow. Therefore, heat transfer between tubes and air is enhanced.
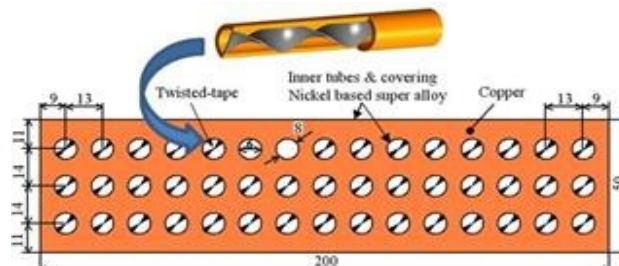
Figure 5. PEGASE embedded tube receiver.

Multistage solar absorber

The solar absorber is multistage. This design fits with the non-uniform distribution of solar flux density at the receiver aperture. The pattern of the absorber modules and the air flow pathway comply with the objective to keep the outer surface temperature of the absorber uniform and close to the maximum allowable value. The air enters the receiver through the absorber modules located in the central zone of the absorber. These modules receive high solar flux density (above 600kW/m^2). The air flows successively through the adjacent absorber stages, in upward and downward directions. The solar flux density decreases along the air pathway. Finally the outlet air temperature reaches 800ºC in the last stages which receive the lowest solar flux density. The resulting design of the solar absorber is presented in Figure 6. The proposed solution also

17

addresses technical issues raised by the fabrication of the modules and their connections to the air distribution and collection tubes.
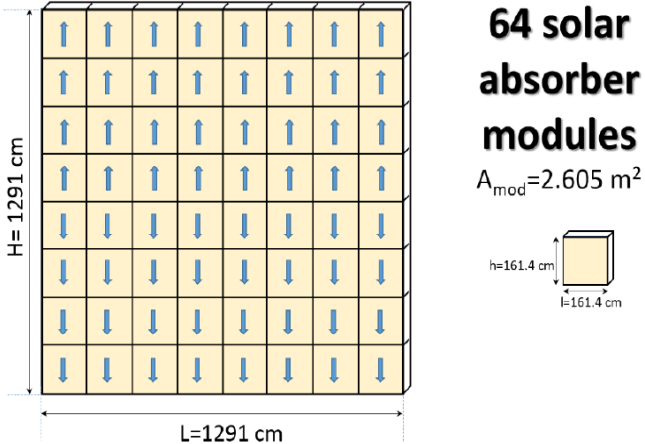
Figure 6. Pattern of the modular solar absorber and flow pathway.

5.2 Cavity

The cavity is made of four flat walls. The aperture plane and the absorber plane are parallel. The aperture area is smaller than the absorber area, thus the radiation losses are reduced when compared to an external receiver. According to the parameters determined in the previous section, the initial design of the solar receiver module is proposed. In this step, only the shape is considered and determined. A sketch of the general design of the solar receiver is presented in Figure 7. The design of the cavity is presented in Figure 8.
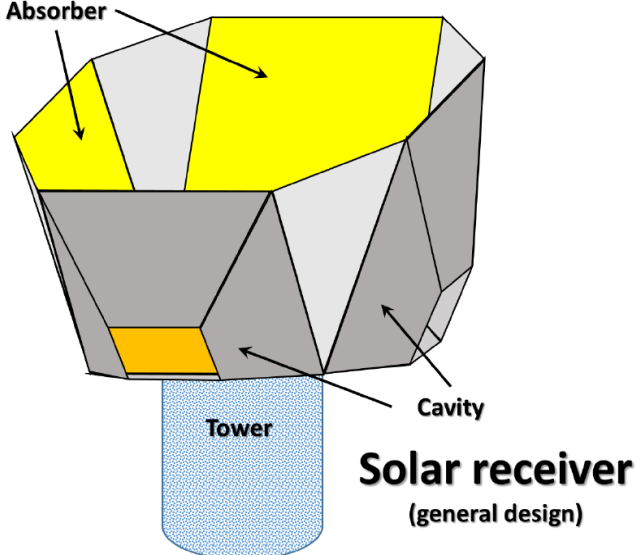
Figure 7. General design of the solar receiver (4 modules).
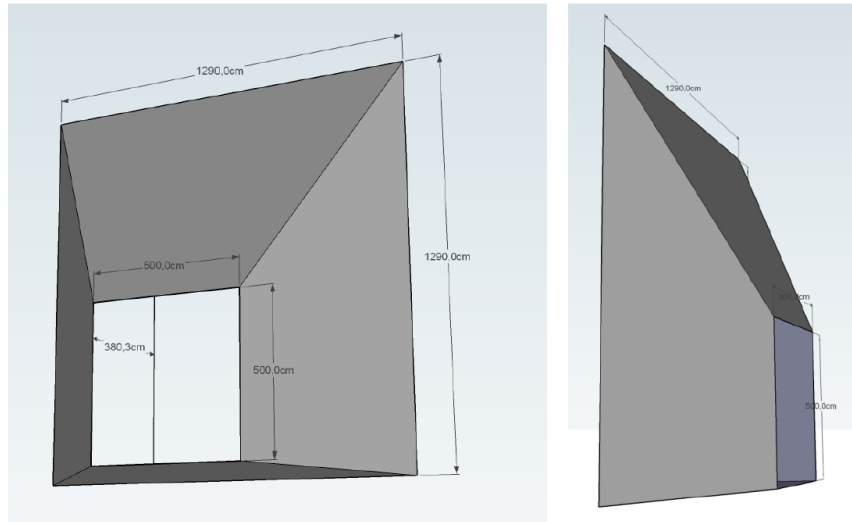
Figure 8. Design of the cavity for one module.

5.3 Solar receiver modelling

Due to the lack of information about the off-design performance of the solar air receiver considered in subtask 12.2.7, a simplified thermal model has been developed.

5.3.1 Assumptions and parameters

For the development of the model the available experimental test results of an absorber prototype have been considered. Main characteristics of this prototype are:

- Total absorber surface (A_{as}) of $1.44m^2$ ($1.2m$ x $1.2m$).
- The absorber surface is composed by 16 modules of air receiver. Inside each module there are 45 pipes with an inner diameter of 6 mm.
- Length and width of modules are 40 cm and 20 cm respectively.
- The deepness of the parallelepiped cavity is 1m.
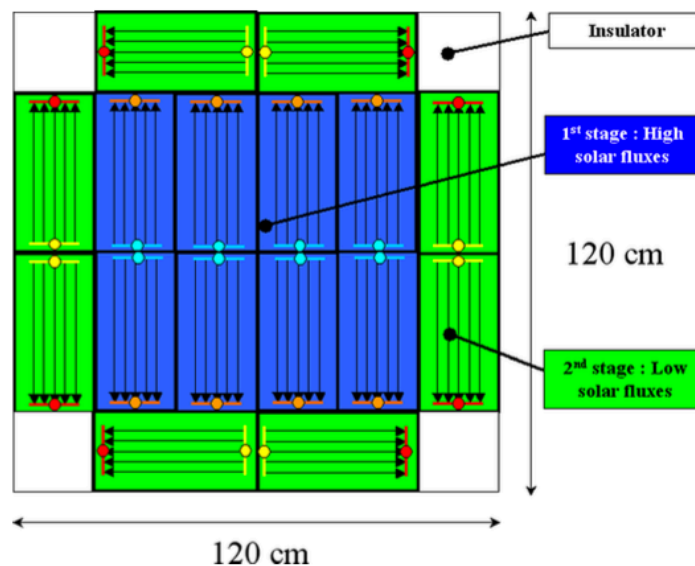
Figure 9. Modules of air receiver forming the absorber surface [4].

The four side walls of the cavity are assumed to be reradiating surfaces.

19

There are other parameters fixed:

- Solar absorptivity of absorber surface (α_{as}): 0.9

- Emissivity of absorber surface (ε_{as}): 0.8

- Air mass flow ($\dot{m}_{air}$): 0.8 kg/s.

5.3.2 Thermal energy model developed

The thermal energy model is based on three heat balances: in the solar absorption surface, in the inner surface of tubes and considering the overall solar absorber, equations (1), (2) and (3) respectively.

$$\alpha_{as}\ \phi\ A_{as} = Q_{rd,as} + Q_{cv,as} + Q_{cd} \tag{1}$$

Where:

- ϕ is the solar flux on the absorber surface [W/m^2].

- $Q_{rd,as}$ is the radiative heat exchanged between the absorber surface and the surroundings (viewed from the aperture area).

- $Q_{cv,as}$ is the convective heat exchanged between the absorber surface and the air inside the cavity. The air inside the cavity is assumed to be at the external (ambient) air temperature.

- Q_{cd} is the conductive heat through the absorber, from the absorber surface to the air pipes.

$$Q_{cd} = Q_{cv,i} \tag{2}$$

$$Q_{cv,i} = \dot{m}_{air}\ Cp_{air}\left(T_{air,out} - T_{air,in}\right) \tag{3}$$

Where:

- Cp$_{air}$ is the air specific heat capacity.
- T$_{air,out}$ and T$_{air,in}$ are the air temperature outside and inside the cavity.

The expressions for heat fluxes are developed below [5]:

$$Q_{rd,as} = \frac{\sigma\left(T_{as}^4 - T_{sky}^4\right)}{\dfrac{1-\acute{U}_{as}}{A_{as}\ \acute{U}_{as}} + \left(F_{as,sky}\ A_{as} + \dfrac{F_{as,lat}\ A_{as}}{2}\right)^{-1}} \tag{4}$$

$$Q_{cv,as} = h_{ext}\ A_{as}\left(T_{as} - T_{ext}\right) \tag{5}$$

$$Q_{cd} = \frac{\left(T_{as} - T_{pipe}\right)}{R_{cd}} \qquad (6)$$

$$Q_{cv,i} = h_{int} \; A_{pipe} \; \Delta T_{rep} \qquad (7)$$

Where:

- σ is the Stefan Boltzmann constant

- A_{as} and A_{pipe} are the absorber and the pipe areas, respectively.

- T_{as}, T_{pipe} and T_{sky} are the absorber surface, the pipe and the mean sky temperatures, respectively.

- $F_{as,sky}$ and $F_{as,lat}$ are the radiation view factors between the absorber surface and the aperture area of the cavity and the absorber surface and the lateral surfaces of cavity, respectively. Considering the geometry used $F_{as,sky}$ and $F_{as,lat}$ are 0.25 and 0.75 respectively.

- h_{int} and h_{ext} are the convective heat transfer coefficients inside the pipes and in the absorber surface respectively.

- T_{pipe} is the average temperature of the pipes.

- ΔT_{rep} is the representative temperature differences between pipe and air mass flow.

- R_{cd} is the conductive resistance of solar absorber. This resistance is considered negligible if it is compared to external and internal heat thermal resistances.

The heat transfer between absorber surface and air flow inside the tubes can be modelled with definition of the overall heat transfer coefficient (U), calculated using this equation:

$$U = \left(R_{cd} + \frac{A_{sa}}{h_{int} \; A_{pipe}} \right)^{-1} \qquad (8)$$

And the overall representative temperature from absorber surface to air flow is calculated using a Logarithmic Mean Temperature Difference (*LMTD*):

$$LMTD = \frac{\left(T_{as} - T_{air,in}\right) - \left(T_{as} - T_{air,out}\right)}{\ln\left(\dfrac{T_{as} - T_{air,in}}{T_{as} - T_{air,out}}\right)} \qquad (9)$$

Finally, the conductive heat transfer can be modelled using next equation:

$$Q_{cd} = U \; A_{as} \; LMTD \qquad (10)$$

The efficiency of solar receiver is calculated using equation 11:

$$\eta = \frac{Q_{cv,i}}{\phi \, A_{as}} = \frac{\dot{m}_{air} \, Cp_{air} \left(T_{air,out} - T_{air,in}\right)}{\phi \, A_{as}} \tag{11}$$

Where:

- Φ is the average air flow.

5.3.3 Simplified black box model

For overall simulation of combined plant, a solar air receiver simplified model is needed in order to not enhance the difficulty of solve the system equation. In this case, a simplified model inspired in efficiency curve of solar collectors is used. The efficiency curve is modelled using the next expression:

$$\eta = \frac{Q_{useful}}{\phi \, A_{as}} = a_0 - a_1 \frac{T_{air,in} - T_{ext}}{\phi} - a_2 \, I \left(\frac{T_{air,in} - T_{ext}}{\phi}\right)^2 \tag{12}$$

Where a_0 and a_1 are the optical efficiency and the linear loss coefficient respectively. Both coefficients are calculated using a linear regression of the efficiency results obtained with the detailed model explained in before section.

The total heat gained by air is calculated using equation (3):

$$Q_{useful} = \dot{m}_{air} \, Cp_{air} \left(T_{air,out} - T_{air,in}\right) \tag{13}$$

To obtain the a_i coefficients, a sensitivity analysis of the solar receiver model variables has been performed; The variables considered and the analysed ranges are:

- $T_{air,in}$ [150,395] ºC
- T_{ext} [10,45] ºC
- ϕ [100, 600] kW/m^2

The efficiency correlation obtained is:

$$\eta = 0.8479 + 22.831 \frac{T_{air,in} - T_{ext}}{\phi} - 0.1515 \, \phi \left(\frac{T_{air,in} - T_{ext}}{\phi}\right)^2 \tag{14}$$

Figure 10 compares the efficiency values obtained with the thermal energy physical model and the simplified black box model for several values of the solar flux between 100 and 600 kW/m^2. The dots represent the physical model and the lines the black box model.
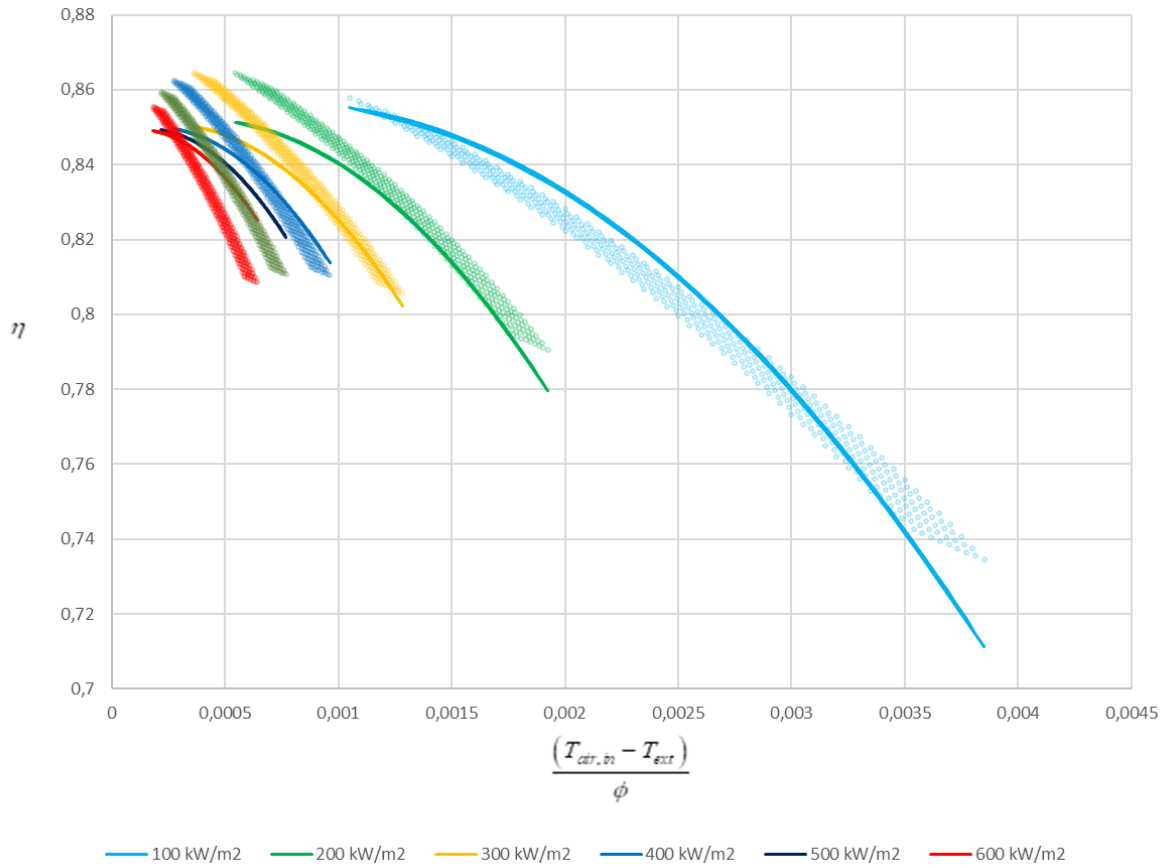
Figure 10. Physical model and black box model comparison.

The average and maximum relative errors in the heat gained between thermal model and simplified model are 0.7 and 3.1 % respectively. If the output air temperature from the solar receiver is compared, the differences are higher: 4.1 % relative error and 17.1 % maximum error. The differences when the output temperature is compared depend on the air mass flow: the higher the mass flow the lower the temperature differences.

5.3.4 Working conditions

Table12 summarizes the working conditions of the receiver considered in the frame of subtask 12.2.7.

Table12. Receiver working conditions.

Parameter	Value
Maximum air temperature	800 ºC
Maximum working pressure	6 bar
Maximum air mass flow	t.b.d. by the scaled up receiver thermal power
Pressure drop	300 mbar
Nominal efficiency	82.5%
Absorbed power	25 MW$_{th}$
Absorber wall temperature	900 ºC
Receiver area	166.7 m^2
Internal heat transfer coefficient	1500 W/m^{2}K
Absorber geometry	12.9m x 12.9m

6 Thermal Energy Storage System

Figure 1 summarises the three plant configurations considered; two of them, B.1 and B.2, include a TES system. In both cases the thermal energy storage capacity considered is 6 hours. In the B.1 configuration a medium temperature TES system located downstream the gas turbine is proposed, while in the case of configuration B.2 a high temperature TES is placed upstream the gas turbine. Throughout this section the main characteristics of both TES systems are described.

6.1 High temperature thermal energy storage system

The high temperature TES configuration B.2 in Figure 1 considers the storage solution proposed by IMDEA Energy in the frame of the subtask 7.4.2 of WP7, STAGE-STE project. The models are described in deliverables 7.8 and 7.14 [6][7]. This proposal is based on sensible heat storage in particles which are heated up by hot air from the receiver using a fluidized-bed heat exchanger. Hot particles are conveyed towards a hot silo for its storage and later this heat is recovered and transferred from the hot particles to the working fluid of the power cycle (air Brayton cycle). After exchanging heat, particles are stored in the cold silo before being conveyed back to the heat exchanger connecting to the air receiver.

The main findings on particles-based thermal energy storage calculations for design point conditions of the Integrated Solar Combined Cycle (ISCC) plant are shown on Table 13. Lower temperature for the air at the outlet of the heat exchanger (HX) due to the inherent energy losses associated to the intermediate TES is translated into an increase in fuel consumption of the burner to reach the targeted temperature and turbine power reduction due to extra pressure losses.

Table 13. Modelling results for high temperature TES under ISCC design nominal conditions.

Parameter	Value
Receiver outlet temperature	800 ºC
HX efficiency connecting with the receiver	95%
Storing particles temperature	760 ºC
HX air outlet temperature	700 ºC
Temperature (target)	1030 ºC
AIR pressure drop along HX pipes	500 mbar

6.2 Medium temperature TES system

For medium temperature energy storage, it has been considered the location of a TES system downstream the gas turbine (and upstream the Rankine bottoming cycle). In this case, thermal energy from hot exhaust gases is transferred to the storage medium (particles) by using fluidized bed heat exchanger configurations following the system proposed by IMDEA Energy. Later another fluidized bed heat exchanger is used for transferring the thermal energy stored at particles to the water/steam of the bottoming Rankine cycle. Table 14 shows the modelling conditions for the medium temperature TES; in this case, the power produced by the bottoming Rankine cycle and, therefore total produced power are reduced due to the lower steam temperature.

Table 14.Modelling conditions for medium temperature TES system.

Parameter	Value
Gas turbine exhaust temperature	600 ºC
HX efficiency for exhaust gases to particles connection	95%
Storing particles temperature	580 ºC
Steam temperature	540 ºC

7 Power block optimization

7.1 Configurations analysed

For the analysis, three different configurations for the bottoming cycle (Rankine) have been considered. The difference between them is based on the number of working pressures for the steam cycle: one, two and three pressures (Figure 11 (a), (b) and (c), respectively). For each pressure: an economizer, an evaporator and a superheater have been considered in the HRSG. In the case of two and three pressures, a reheater for the intermediate pressure has also been considered. In all cases, the condenser has been coupled to a cooling tower (wet cooling).
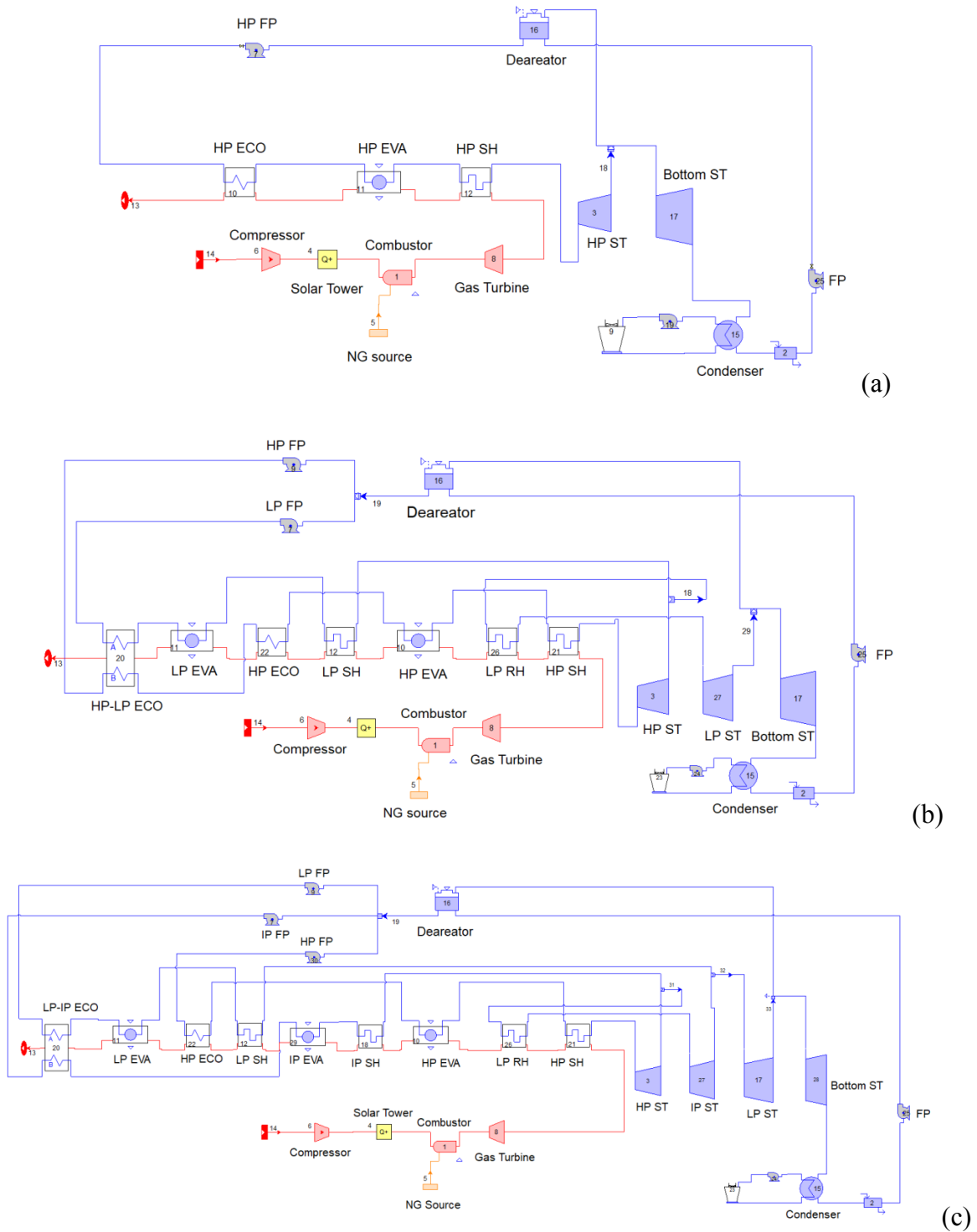
Figure 11. Integrated Solar Combined Cycle (ISCC) Power block configurations: (a) One pressure, (b) Two pressures, (c) Three pressures.

7.2 Simulation results and discussion

The schemes shown in the previous section have been simulated in two ways; firstly, considering an exclusive contribution of thermal energy through the solar thermal receiver (solar mode), and secondly, a mixed thermal contribution by solar energy and natural gas (fueled mode), via a combustor located downstream the solar receiver and upstream the gas turbine; inlet natural gas mass flow has been determined for reaching gas turbine outlet

26

temperature of 600ºC (typical temperature in conventional Combined Cycles (CC) [8]). Thermoflex software tool has been used to perform the power block analysis [9].

Simulations results are presented on Figure 12 to Figure 14 where the variation of the net combined cycle efficiency is represented against the steam pressure for each of the three configurations of the power blocks described on Figure 11. Parametric studies on Rankine cycle steam pressures were performed for the three plant layouts shown on Figure 11 both for solar mode and fueled one and covering the whole pressure range from 10 bar to 110 bar. Figure 12 to Figure 14 show the power block net efficiencies for both the solar and fueled mode. Cycle net efficiency has been calculated according to equation (15).

$$Net\ efficiency\left(\%\right) = \frac{P_{block}}{Q_{sun} + m_{NG} \cdot \text{LHV}_{NG}} \cdot 100 \tag{15}$$

Where P_{block} is the electric net power produced by ISCC, Q_{sun} is the thermal energy gained by air in the solar receiver, m_{NG} is the mass flow of natural gas consumed and LHV_{NG} is the lower heating value of natural gas.

In general, optimum steam pressures found for all configurations are lower in the solar mode than in the fueled mode, this is because the gas turbine outlet temperature for the solar mode is 437.7ºC (gas turbine inlet temperature limited to 800ºC due to air receiver performance). However, for the fueled mode, exhaust gases at 600ºC can be achieved by fuel assistance (turbine inlet temperature: 1031ºC). This temperature difference is the reason for the different pressure levels of the steam Rankine cycle. It is also observed that net efficiency slightly depends on the working conditions of the bottoming cycle (±2% for most of the configurations). The parameters that primarily affect cycle efficiency are the inlet and outlet temperature of gas in the Gas Turbine (but the outlet temperature is given by pressure ratio and turbine inlet temperature). The higher the temperature the higher the topping cycle (Brayton) efficiency according to the Second's Law of thermodynamics but in both modes (solar and fueled), these temperatures have been fixed since the pressure ratio cannot be increased. As it can be observed, the two-pressure level Rankine cycle configuration shows higher efficiency than one and three-pressure levels, above 47% for fueled model and 40% for solar mode (lower temperature available). It was also found for the solar mode that increasing the steam pressure of the HP turbine with respect to the optimum values of 15 bar (one-pressure), 40 bar (two-pressure) and 60 bar (three-pressure) will worsen the combined cycle optimum efficiency, due to a higher consumption of water pumps. For the fueled mode, slightly higher pressures were found as the optimum values providing cycle peak efficiency while going beyond that pressure will not impact on cycle net efficiency. Steam pressure levels found in fueled mode are coherent with real CC fed exclusively with natural gas [10]. Cycle efficiencies of ISCC with the assumed boundary conditions are far from real CC by two reasons: Firstly, the inlet temperature of the gas in the gas turbine (typical values are between 1300-1400 ºC), and secondly, the low gas pressure ratio in the Brayton Cycle (in commercial CC is in the range 17-25). As mentioned above, there is a limitation in the maximum temperature and pressure at the inlet of Gas Turbine due to solar receiver specifications which reduce the achievable CC efficiency.
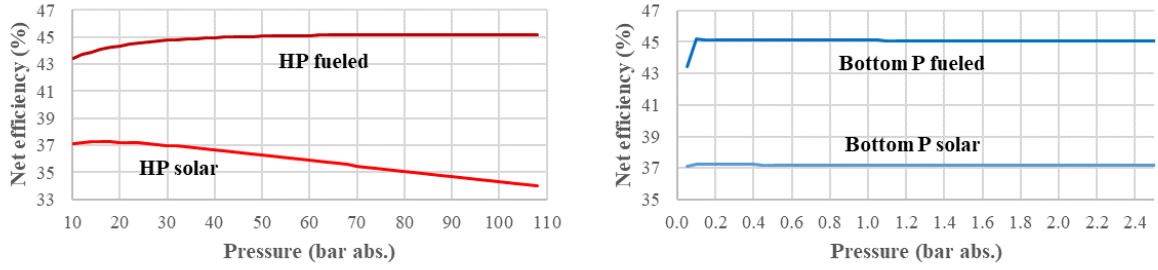
Figure 12. Net efficiency of ISCC configuration a (one-pressure level). Left: High pressure steam. Right: Bottom pressure steam.
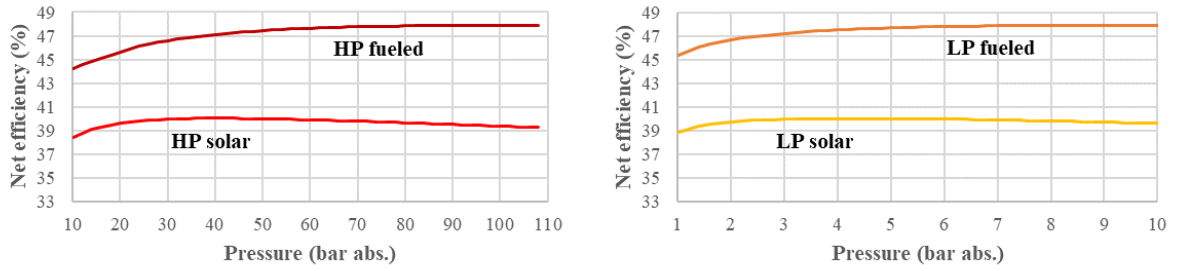

Figure 13. Net efficiency of ISCC configuration b (two-pressure level). Left: High pressure steam. Right: Low pressure steam.
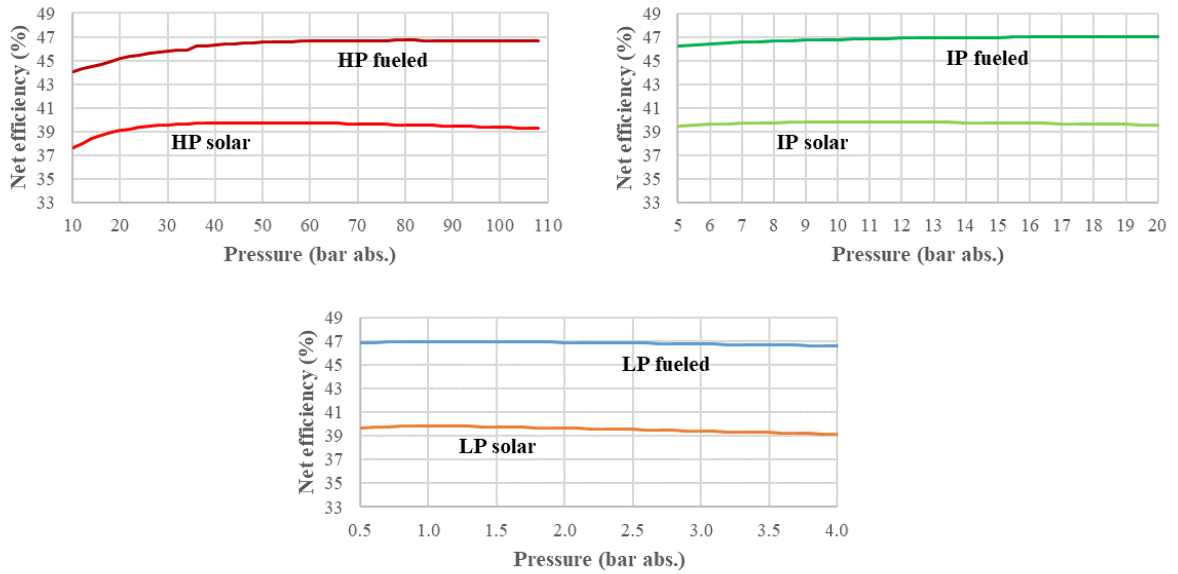

Figure 14. Net efficiency of ISCC configuration c (three-pressure level). Left: High pressure steam. Right: Intermediate pressure steam. Down: Low pressure steam.

Table 15 and Table 16 show the optimum pressures for each configuration, the net cycle efficiency obtained and the net power produced by the ISCC. On average, the efficiency of the ISSC in fueled mode is 7 points higher compared to the same ISCC in solar mode. Also, it has been demonstrated that a two pressure-levels Rankine cycle has a higher efficiency than the same with higher working pressures when the cycle is the bottoming cycle of a CC power plant. This conclusion holds for both operation modes, solar and fueled. Table 16 also shows the percentage of thermal energy introduced by solar irradiation to the whole system. As it can be seen, the contribution made by solar energy varies between 54 % and 56 %.

Table 15. Optimum operating pressures for ISCC only fed by solar energy.

Configurations	PRESSURE (bar abs.)				Cycle efficiency (%)	Net Power (MW$_e$)
	HP	IP	LP	Bottom P		
a	16.5	-	-	0.1	37.2	37.2
b	38	-	4	0.1	40.0	40.0
c	48	9.5	1	0.1	39.7	39.8

Table 16. Optimum operating pressures for ISCC fed by solar energy and natural gas.

Configurations	PRESSURE (bar abs.)				Cycle efficiency (%)	Net Power (MW$_e$)	Solar contribution (%)
	HP	IP	LP	Bottom P			
a	80	-	-	0.1	45.6	68.6	54.2
b	77	-	8	0.2	47.8	71.8	55.4
c	103	17.5	1.5	0.2	47.0	70.6	56.2

8   Plant modelling software

To achieve the objective of subtask 12.2.7 it is necessary to develop a tool able to simulate the behaviour of the plant whose configurations have been subject of study in the frame of WP12 and described in the previous sections of this document.

From the beginning of this subtask it was desired the definition of a common platform for solar plant modelling inside the STAGE-STE project, because modelling tasks will be performed as well across other work packages, mainly WP7 (subtask 7.4.2) and WP9 (task 9.4). Currently, there is not a single modelling platform able to model the behaviour of all the components of the solar power plant (heliostat field, central receiver, storage, power block and auxiliaries) with the required level of detail neither for design conditions nor for transient/annual scenario. For this reason a combination of modelling tools is needed.

In the initial stage of this subtask, the possible modelling tools were evaluated and it was concluded that the modelling tool should fulfil the following requirements:

- Simplicity
- Modularity
- Flexibility
- Accuracy
- Calculation speed
- Dynamic behaviour

Regarding the optical analysis of the heliostat field, the following modelling tools were discussed:

- Tonatiuh
- TracePro

- WinDelsol
- SolarPILOT

For the solar loop and power block modelling, the following software applications were discussed:

- Ebsilon Professional
- TRNSYS
- MATLAB in-house code
- EcoSimPro

For the power block stand-alone calculation, the following software was identified:

- Thermoflex

It was agreed to choose a combination of the above-mentioned modelling tools for the overall plant modelling according to the requirements previously discussed. In-house MATLAB code was the preferred option for solar plant and power block modelling at the design point. This software allows its connection to other modelling tools such as TRNSYS [11] which was selected to simulate annual performance. As it can be seen on Figure 15, the working methodology has been integrated into a main MATLAB routine managing these three blocks or modules in a forward direction according to the plant specifications given. Detailed heliostat field calculation and optimization was performed using SolarPILOT software [2]; the MATLAB program was fed with the solar field efficiency matrix calculated by SolarPILOT. Thermoflex software [9] was used for detailed selection and optimization of operative conditions for the power block.
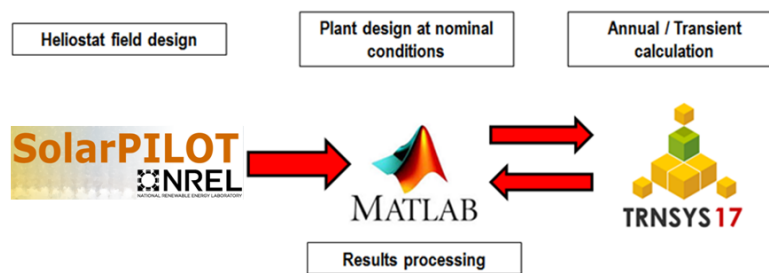

Figure 15.Modelling Methodology

Mathematical models for the solar plant components have been coded into MATLAB platform in order to optimize plant operative conditions. Once MATLAB has successfully calculated the overall design of the plant operative conditions, the annual performance of the plant will be modelled using TRNSYS. TRNSYS has been chosen for dynamic modelling due to its flexible simulation environment, reduced computational times, coupling possibilities with MATLAB, specific code libraries allowing the creation or modification of new components and its dedicated solar components from STEC library [12].

MATLAB routine has been prepared to transfer the required input data obtained from the design process to TRNSYS software in order to perform annual modelling. Once the annual simulation

had been completed, MATLAB routines have been programmed to load the TRNSYS simulation outputs generated into text files to proceed with the post-processing task.

9 Simulation results

9.1 Design conditions

Table 17 shows the modelling results for the combined cycle power at design conditions. These numbers have been obtained following the optimization processes and for working conditions described above.

Table 17. CSP plant design point conditions.

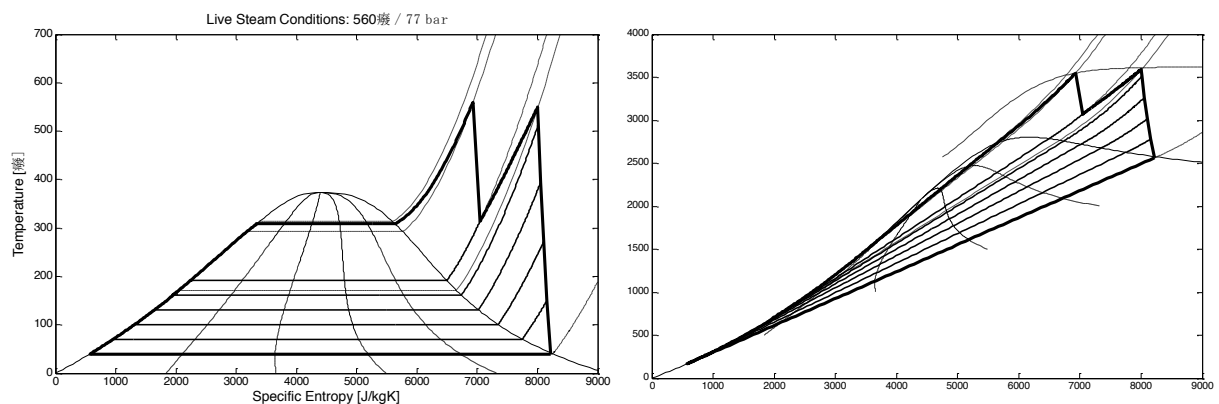| Parameter	Design efficiency		
	B1	**B2**	**B3**
Solar field efficiency	66.4%	66.4%	66.4%
HX efficiency	93.8%	94.0%	95.0%
Receiver thermal efficiency	83.8%	83.8%	83.8%
Power block efficiency	47.4%	47.2%	47.9%
Sun-to-electricity efficiency	24.8%	24.7%	26.6%

Figure 16. Power cycle optimized working conditions. Temperature-entropy diagram (a). Enthalpy-entropy diagram (b).

9.2 Annual performance

The analysis of the annual performance of the different CSP plants configurations using TRNSYS modelling is presented in this section. The overall plant scheme layout is shown in Figure 17.
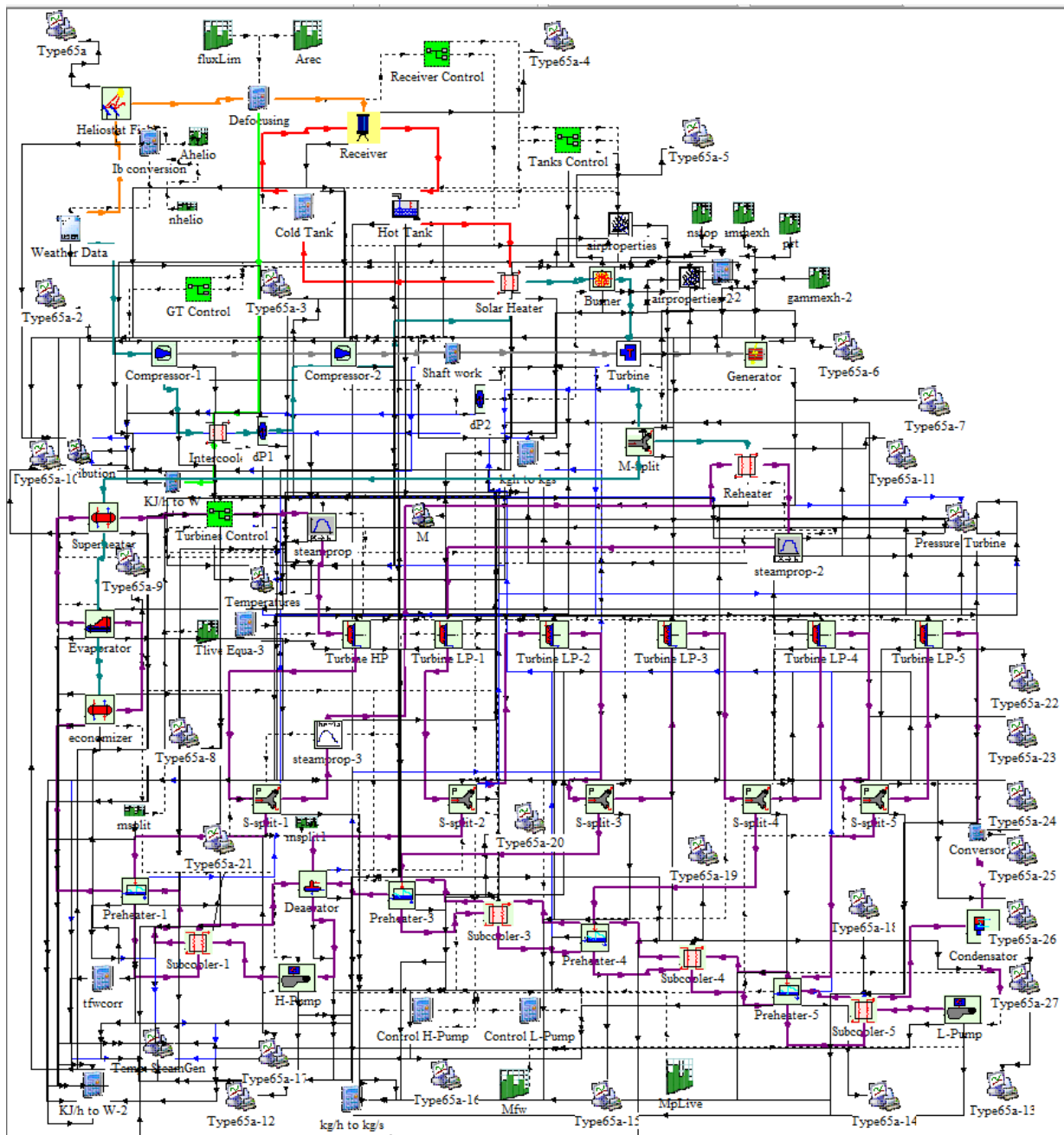
**Figure 17. Power plant layout (TRNSYS layout).**

The optimized heliostat field matrix provided in solar field optimization section has been used for the annual modelling of the solar plant as well as the simplified thermal model of the receiver described in the central receiver optimization section. Power block layout and optimized operating pressures from the power block optimization section have been set for the power cycle. The annual performance modelling of the solar plant uses a typical meteorological year for Seville with a time resolution of 10 minutes. Heliostat defocusing strategy has been included in order to limit the peak flux reaching the receiver below 600 kW/m² that was determined as the safety limit for receiver material. Natural gas combustor hybridization has been implemented in order to compensate for insufficient thermal power during cloudy events and to ensure constant electricity production of the power block.

9.2.1 Combined cycle with no thermal energy storage (case B.3)

As it can be observed in Figure 18, the combined cycle power block is working at constant electric power determined for design point conditions (around 70MWe). To achieve constant power, natural gas assistance is required to mitigate fluctuations of thermal power reaching the receiver and thermal losses at the steam generator that is connecting the air Brayton topping cycle and steam Rankine bottoming cycle. Natural gas assistance also contributes for power block efficiency improvement, as it was discussed in section 7 since it increases the available thermal power for the gas turbine.
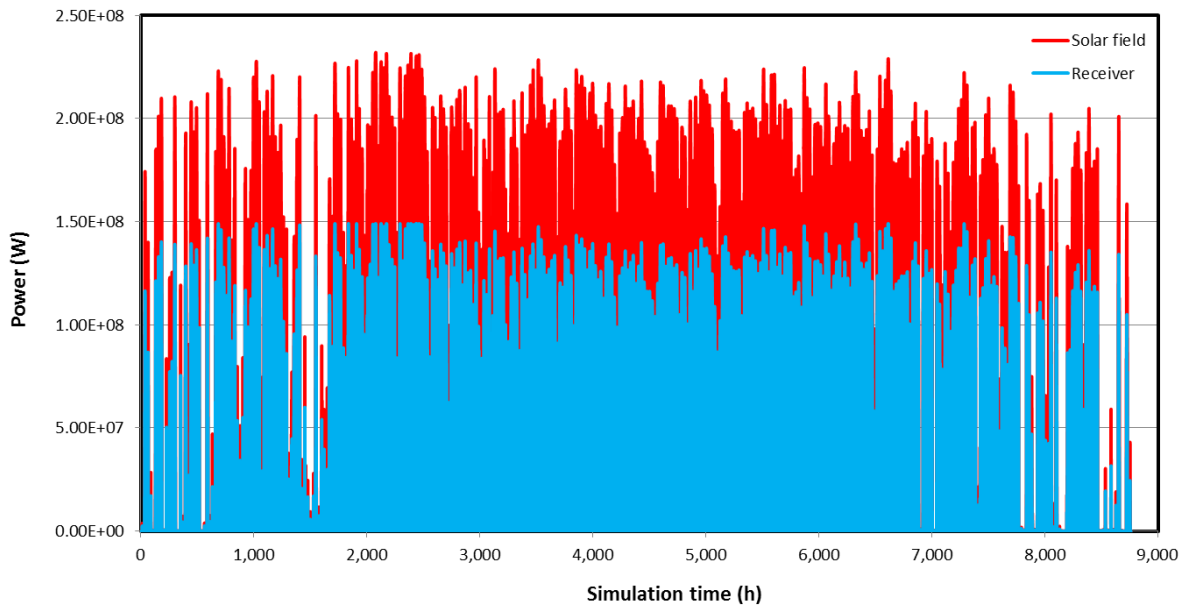
a)   Power reaching the solar field (red) vs. Thermal power reaching the receiver (blue)
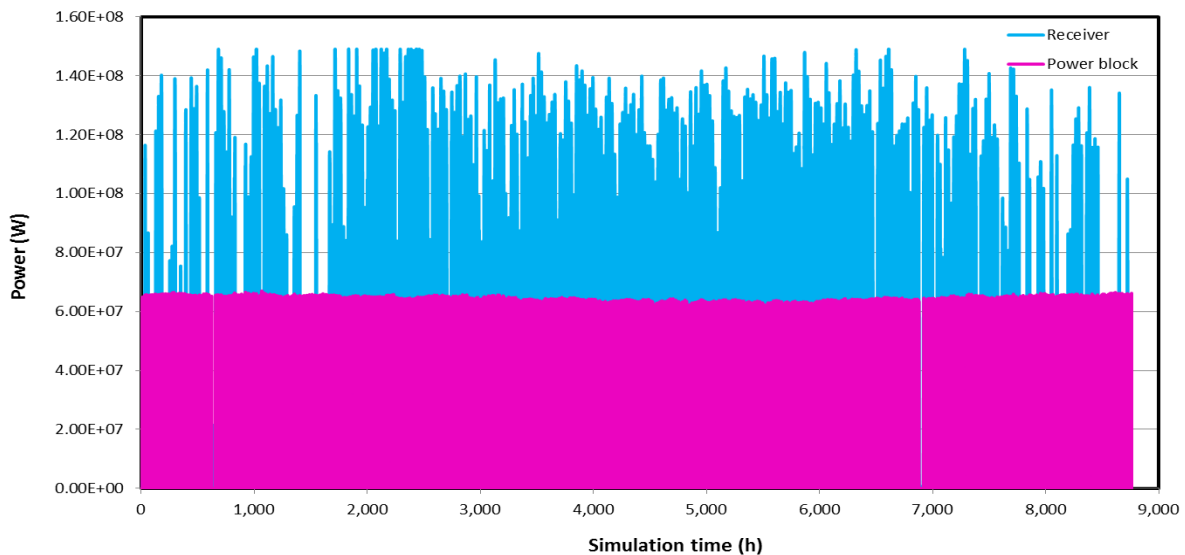
b)   Thermal power reaching the receiver (blue) vs. Electrical power produced by the power block (pink)

Figure 18. Solar plant annual performance.

The following figure shows a detail of the instantaneous thermal power absorbed at the receiver (red line) and total electricity produced by the gas turbine and steam turbine (blue line).
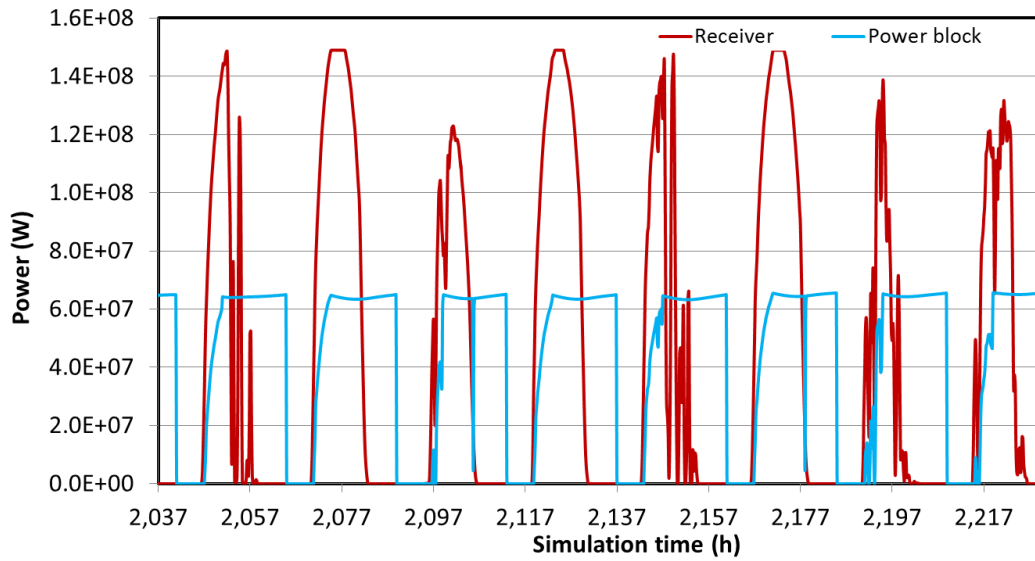
Figure 19. Detailed view of power block electricity production (blue) and absorber thermal power at the receiver (red).

Solar receiver efficiency throughout several days can be found in the following figures.

a) 15th March

b) 27th April

c) 21st June

d) 21st September
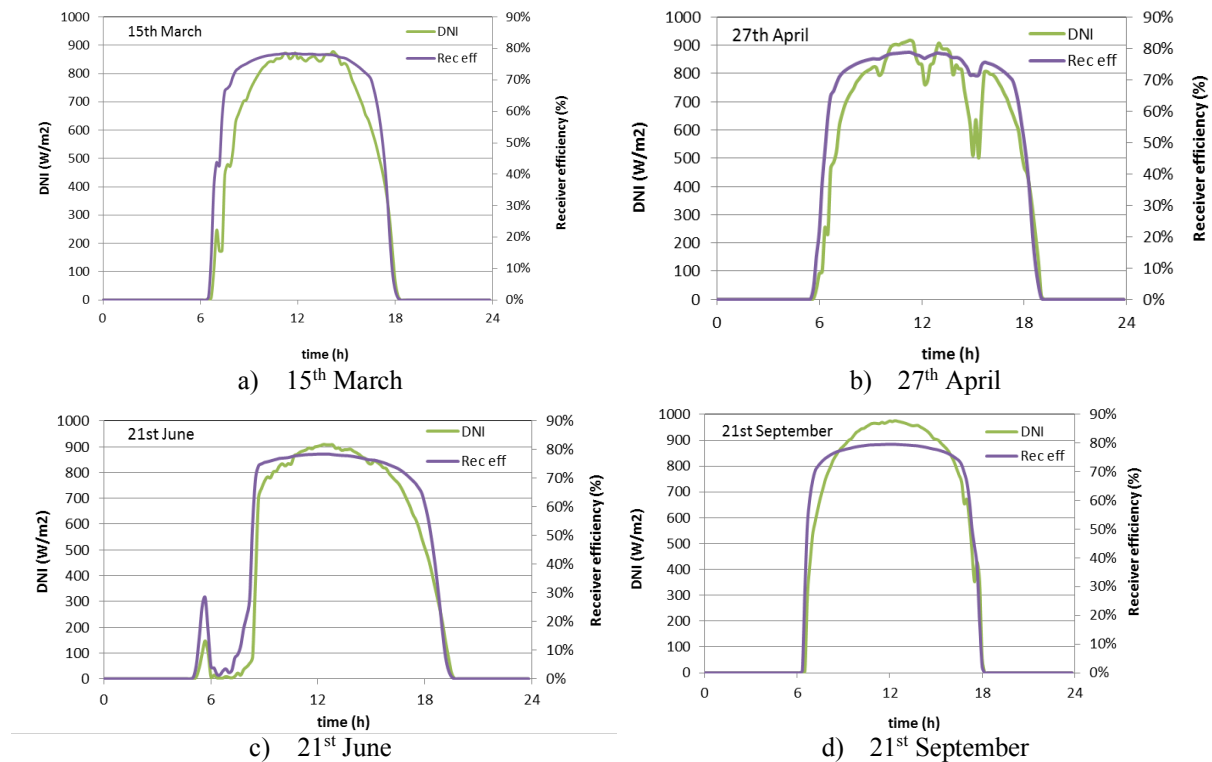
Figure 20. Receiver thermal efficiency for four example days.

As it can be observed from Figure 20, receiver thermal efficiency varies from 70% to 80% for most of modelling conditions as it was predicted from receiver correlation. Nevertheless, this is leading to an annual efficiency of the solar receiver of almost 74%. Efficiency calculations are based on the mathematical correlation that was derived for the receiver prototype. It is expected that the scaled-up receiver will show higher efficiencies due to scaling-up effects.

Table 18. Solar plant annual efficiency – Configuration B.3

Parameter	Value
Solar field	60.4%
Receiver	74.0%
Exchanger	95.3%
Power cycle	42.3%
Sun-to-electricity	17.1%
Solar share	26.3%

Figure 21 shows the instantaneous thermal power reaching the receiver (red), thermal power released by the fuel (orange), thermal power at the outlet of the combustor (green) and net electricity generation of the power block (blue),in order to reach the targeted steady electric power that was determined through the optimization process. As it can be observed from the annual simulations, the solar contribution is a small fraction of the total thermal power required for the operation of the combined cycle at optimum conditions. This can be confirmed from the small variations on the thermal power that is provided by the burner along the year.

a) Winter days   b) Spring days

c) Summer days   d) Autumn days
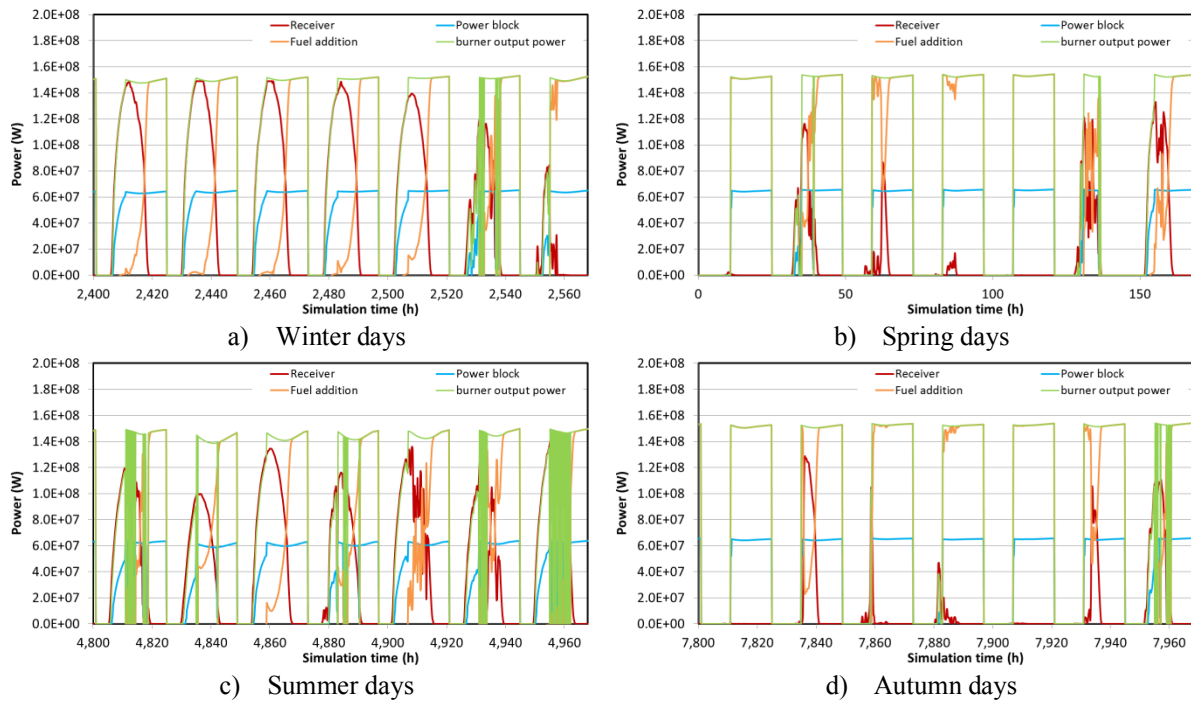
Figure 21. Instantaneous modelling results for annual simulation (different weeks of the year have been represented) efficiency.

9.2.2 Combined cycle with thermal energy storage upstream the gas turbine (case B.2)

In this case, the high temperature energy storage system is located downstream the air receiver. The particles-based TES system proposed on STAGE-STE WP7 – D7.14 [7] has been coupled to the solar plant described in this report. Specifications shown on Table 13 have been considered for the particles-based TES modelling. The main differences with the no-TES configuration are related to the gas turbine performance. On the one hand, the power output

will be lower due to the air pressure losses introduced by TES system. On the other hand, lower air temperature will result upstream the combustor due to the thermal losses of TES system. This will lead to an increase of fuel consumption at the combustor in order to achieve the targeted temperature at the gas turbine inlet (1030ºC). Both, lower pressure and temperature, will result into lower net power production and higher fuel consumption.

The combined cycle layout and working conditions have been optimized for the design point conditions of the case without thermal energy storage. In that case, net power production was about 70 MW$_e$ which in turn resulted into a solar share of 55%. Configurations B.1 and B.2 include thermal energy storage but heliostat field and receiver designs are the same of configuration B.3 (no storage). This will require higher fuel consumption for maintaining steady production at design conditions (70 MW$_e$) which will result in poor solar contribution of the power plant. Among several strategies that could be proposed for the integration of thermal energy storage to the solar plant, the case of storing half of thermal power produced at the receiver has been analyzed. In this case, steady electricity production of the plant will be extended after the sunset using stored thermal energy (as it can be seen in Figure 24-e).

In this scenario, storage tanks are empty at the early hours of the day for plant start-up. During that time, the power plant will run as if there was not storage system. The main side effect of this approach will be that weather fluctuations at morning hours will affect turbine performance which will work in transient mode (as it can be seen in detail on the left hand side of Figure 24-e). Auxiliary back-up burner will take an active role during the whole operation of the plant ensuring constant target temperature (1030 ºC) at gas turbine inlet. After sunset, the power plant will continue operating at constant power output until the hot tank is at 5% of its capacity. Cold start-ups of the turbine will take place once a minimum thermal power of 25% of the nominal load is reached. This period will last 30 minutes; 50% of thermal power will be needed for the warm-up and will not be transformed into electricity. Warm stand-by situations have been contemplated in the model as well but without extra energy required to maintain this operating condition.

Figure 22 shows the instantaneous thermal power reaching the receiver along the year (blue) and power reaching the solar field (red). As it can be noticed, both power signals are the same as the ones found for no-TES case. This is because neither the heliostat field nor receiver designs were altered when introducing TES.
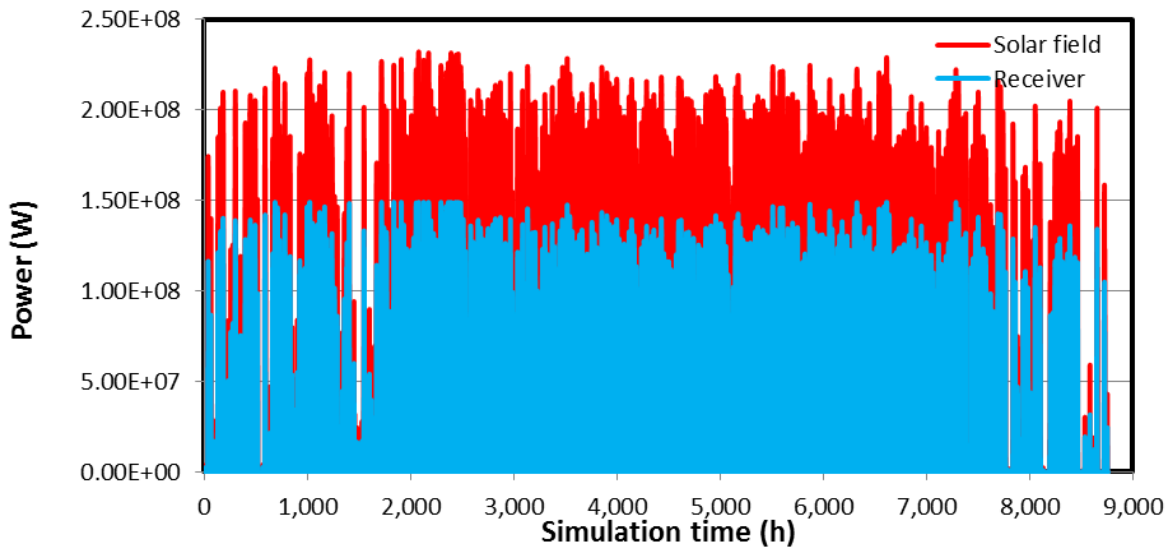
Figure 22. Annual instantaneous power reaching the solar field and the solar receiver.

Figure 23 shows the thermal power reaching the receiver (blue) and net power production of the power block (pink). Apart from the net power production reduction, the power cycle efficiency is reduced as introducing particles-based TES system is translated into power reduction of the gas turbine (lower pressure ratio).
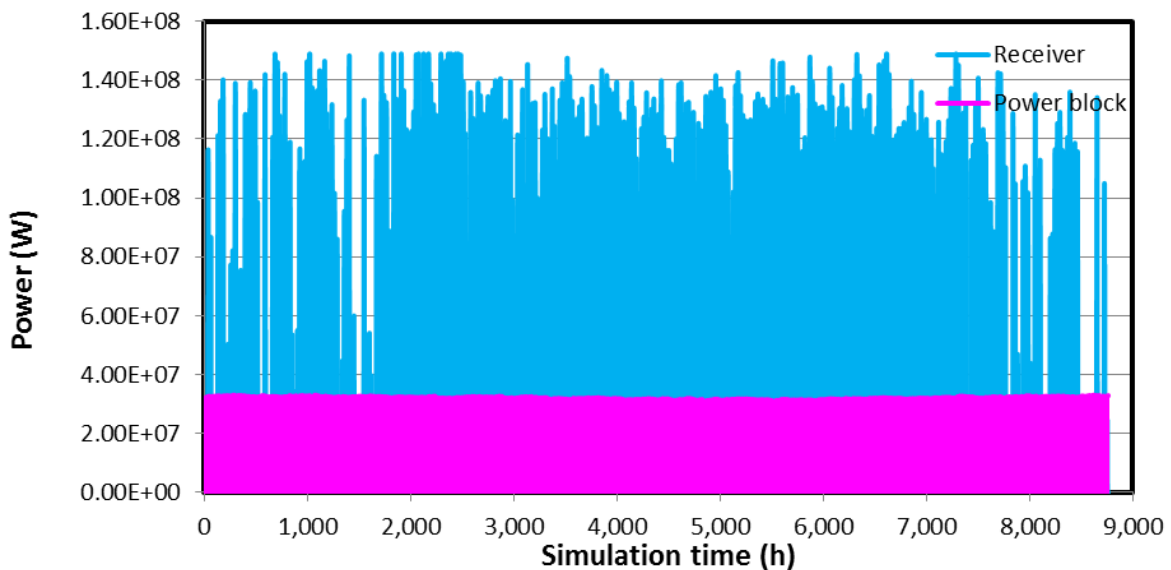

Figure 23. Annual instantaneous power reaching the solar receiver and power produced by the power block.

Figure 24 shows the instantaneous power of different components of the power plant along the year. One week of each season has been selected for comparison purposes. Electricity net production is represented in blue, instantaneous thermal power reaching the receiver in red and external thermal power supplied by gas burner in green. As it can be seen, the power output of the power block is reduced compared to the case of having no TES. This is due to the lower air mass flow circulating through the gas turbine due to the high temperature TES. As it can be observed, transient events on the receiver (selected first day from autumn or selected second day from winter) are not affecting power block net electricity production based on fuel consumption. Detailed operation mode shown for a given day (Figure 24e, corresponding to the

38

2nd day) shows the interaction between storage system, combustor and power block. As it can be observed, The TES is charged (black line) using half of the available solar thermal energy produced at the receiver while the other half is diverted to the power block. Due to the fact that thermal power reaching the power block is not enough for ensuring steady electricity production, external heat addition is required from the burner (orange line) which also compensates oscillations from the receiver. After sunset, storage tanks are discharged (dotted line) for maintaining the power output together with the contribution of the external burner.
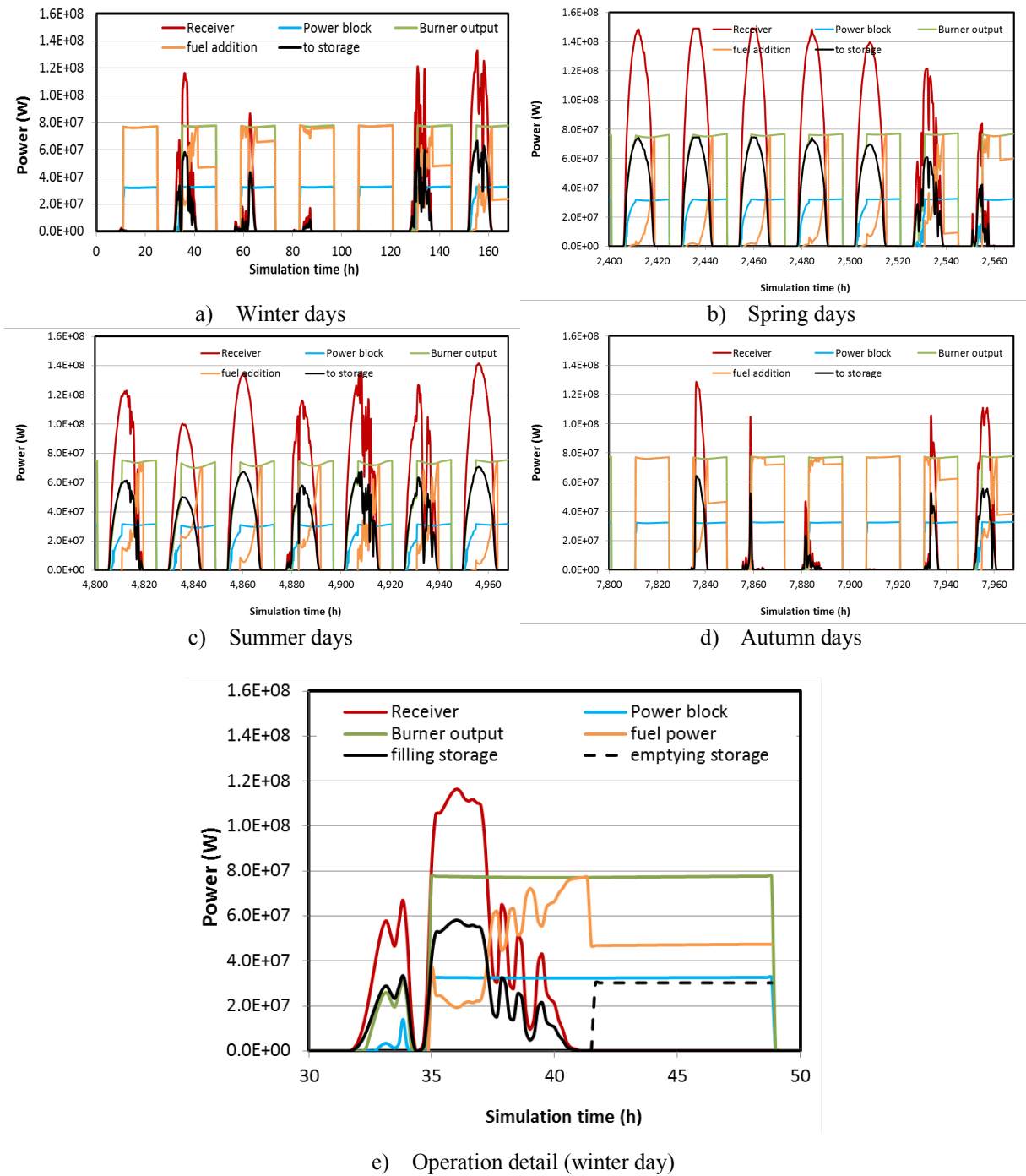

a)   Winter days

b)   Spring days

c)   Summer days

d)   Autumn days

e)   Operation detail (winter day)

Figure 24. Instantaneous modelling results for annual simulation (different weeks of the year have been represented).

As it can be observed from the Table 19, the solar share increases compared to case B.1 (no-TES) and, consequently, the fuel consumption decreases. In addition, the sun-to-electricity efficiency slightly improves compared to the no-TES case due to the improvement of the receiver efficiency which compensates the slight reduction of the power cycle efficiency due to the lower pressure ratio of the gas turbine.

Table 19. Solar plant annual efficiency – Configuration B.2.

Component	Annual Efficiency
Solar field	60.4%
Receiver	78.4%
Exchanger	94.9%
Power cycle	41.8%
Sun-to-electricity	18.8%
Solar share	38.8%

9.2.3 Combined cycle with thermal energy storage downstream the gas turbine (case B.1)

In this case, the thermal energy storage is located downstream the gas turbine exhaust. Particles-based thermal energy storage system is considered with working conditions summarized in Table 14. Exhaust gases from the gas turbine are at temperature above 600ºC. Hot air is used for heating-up a fluidized bed of particles that is working as intermediate energy storage system. Hot particles are later transferring the stored heat to the water/steam of the bottoming Rankine cycle using a fluidized-bed heat exchanger. Due to thermal losses and inefficiencies of the heat exchangers, the maximum temperature for the steam of the Rankine cycle is reduced from 560ºC to 540ºC.

Figure 25 represents instantaneous power reaching the solar field (red), solar receiver (blue) and net power produced by the power cycle (pink). As it can be observed, thermal performance of solar field and air receiver do not change as the designs used in all three cases are the same.
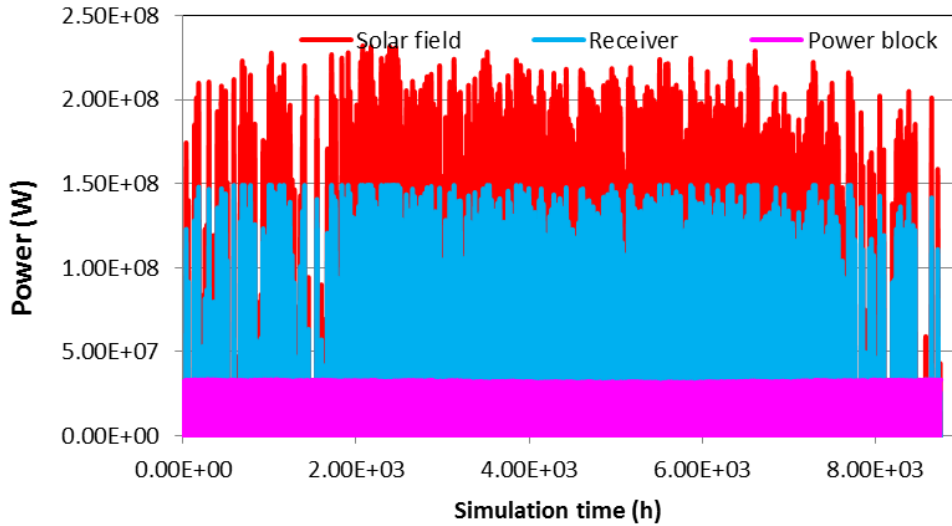
Figure 25. Annual instantaneous power reaching the solar field and the solar receiver.

Figure 26 shows the instantaneous thermal performance of different components of the power plant: thermal power at the auxiliary burner (green), thermal power absorbed at central receiver (red) and net power production (blue). As it can be observed, net power production keeps constant despite solar radiation variations thanks to fuel burning in the auxiliary burner (orange). Electricity production is extended after the sunset by using thermal energy stored.

a)   Winter days

b)   Spring days

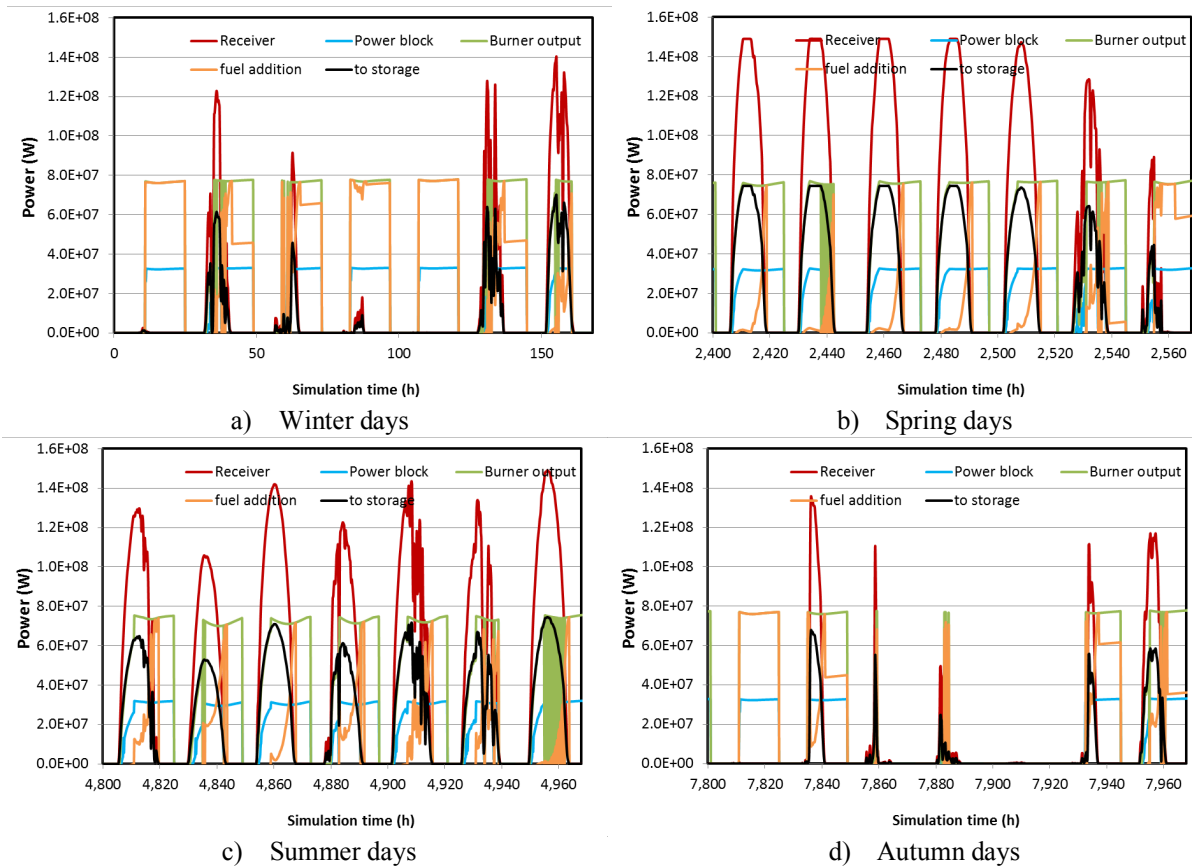c)   Summer days

d)   Autumn days

Figure 26. Instantaneous modelling results for annual simulation (different weeks of the year have been represented).

Table 20 shows annually averaged efficiency of different components of the solar power plant.

Table 20. Solar plant annual efficiency – Configuration B.3.

Component	Annual Efficiency
Solar field	60.4%
Receiver	78.8%
Exchanger	95.0%
Power cycle	41.8%
Sun-to-electricity	18.9%
Solar share	42.2%

10 Discussion

The following table shows a comparison of the three cases analysed in terms of cumulative electricity production and thermal output of the burner (upstream the gas turbine). Electricity production of case B1 (medium temperature TES) is slightly lower than in case B2 due to the thermal losses from TES and steam generator system that reduce power production of the steam turbine. As it can be observed, electric production from case B3 (no TES) is higher than B1 and B2 because this case was designed for maximizing combined cycle efficiency given operating constraints imposed by the receiver (maximum pressure) and burner (maximum temperature). This resulted into high electric power output from the combined cycle (71 MW). However, for TES scenarios (B2 and B1) the power block operation for producing the same electric power requires a high fuel consumption at the burner, thus resulting in a low solar fraction. Therefore, the combined cycle will run at a lower power despite the reduction in efficiency.

Table 21. Cumulative electricity production and thermal output of the burner.

Parameter	Cummulative value		
	B1	**B2**	**B3**
Burner output thermal energy(MWh)	3.94 E5	4.30 E5	7.76 E5
Gas turbine electric energy(MWh)	9.99 E4	1.03 E5	1.97 E5
Steam turbine electric energy(MWh)	6.48 E4	7.45 E4	1.31 E5
Electric energy generated(MWh)	1.65 E5	1.77 E5	3.28 E5

11 Summary and Conclusions

The objective of Subtask 12.2.7 was to identify a representative high concentration optical system based on the results of the collaborative work carried out in the frame of the STAGE-STE project and, more specifically, of WP12, and perform its detailed design and analysis.

Regarding the collector system (heliostat field and solar receiver) the most relevant outcomes of WP12 have been:

- development of a number of prototypes of small-size heliostats;
- development of heliostat field design and optimization tools and methodologies;

- design and testing of a flat-plate pressurized air receiver (prototype module);
- design and testing of a molten salt receiver with integrated storage (prototype).
- particle-based thermal energy storage.

Partners agreed to use the pressurized air receiver module concept because a more detailed assessment of this module, including experimental test results, was available. Since the up-scaling concept of the molten salt receiver is not defined yet, it was decided to opt for the pressurized air receiver. Its modularity simplifies scalability.

With this basis, two options were initially identified:

- Option A: multi-tower configuration, each tower including a gas turbine without thermal energy storage.

- Option B: single tower, with surrounding field and multi-cavity receiver, connected to a hybrid (solar-gas) combined cycle. Three configurations are considered within this option:

  o Thermal Storage System (TES) fed by gas turbine exhaust and feeding the heat recovery steam generator (HRSG); the combustor is in series with the receiver output (Option B.1 in Figure 1).

  o TES fed by the receiver thermal output and feeding the gas turbine; a gas combustor is in series with the TES output to provide stability (Option B.2 in Figure 1).

  o No TES; the combustor is in series with the receiver output (Option B.3 in Figure 1).

The first option was discarded because of its relatively low efficiency compared with the solarized combined cycle option.

The receiver concept consists of 4 modules of 25 MW thermal each, integrated into the corresponding cavities. Each module is oriented in a different direction (N, S, E, W) and receives the solar flux concentrated by the corresponding section of the heliostat field.

The resulting collector field generates 100 MW$_{th}$ in design conditions. The integration of this collector field in each of the three configurations has been analysed, using different tools to optimise the configuration of the power cycle.

Of the three configurations B.3 (no thermal energy storage) presents a low solar share, as expected, and the lower solar to electricity conversion efficiency. B.1 and B.2 show similar annual solar to electricity conversion efficiency (close to 19%), but the solar share of B.1 (TES downstream the gas turbine) is higher (42.2% vs 38.8%).

These results show the technical feasibility of the configurations analysed. However, the results hardly improve the performance already offered by the state-of-the-art technology (molten salt towers) in terms of efficiency, at the cost of a significant consumption of natural gas. It is to be noticed that the high efficiency potential of combined cycles is not fully exploited with the proposed configurations because of the constraints, in terms of maximum temperature and pressure ratio, of the flat-plate air receiver considered. Further developments should be carried

out for the development of solar air receivers capable to with stand higher working pressures and temperatures which in turn will substantially improve the efficiency of the power block.

12 References

[1]   Kisler, B. L. A user's manual for DELSOL3: A Computer Code for Calculating the Optical Performance and Optimal System Design for Solar Thermal Central Receiver Plants, SAND86-8018. Sandia National Laboratories, Albuquerque, NM, 1986.

[2]   https://www.nrel.gov/csp/solarpilot.html(accessed 20 December 2017).

[3]   Vrinat, M., Ferrière, A., Sans, J-L., Daniel, M., Mercier, P., Pra, F. Experimental qualification of a high temperature air solar absorber based on compact heat exchanger technology. 15th International SolarPACES Symposium on Solar Thermal Concentrating Technologies. Berlin, 2009.

[4]   Grange, B., Ferrière,A., Bellard, D., Vrinat, M., Couturier, R., Pra,, F., et al. Thermal Performances of a High Temperature Air Solar Absorber Based on Compact Heat Exchange Technology. ASME Journal of Solar Energy Engineering 2011, Vol. 133, ISSN 0199-6231.

[5]   Bellard, D., Ferrière, A., Pra, F., Couturier, R. Experimental characterization of a high-temperature pressurized air solar absorber for the PEGASE project. 18th International SolarPACES Symposium on Solar Thermal Concentrating Technologies. Marrakech, 2012.

[6]   Report Assessment of fluidized power beds feasibility to high temperature thermal storage. Deliverable D7.8. EMDESK.

[7]   Integration of advanced thermal storage systems in central receiver solar power plants. Deliverable D7.14. EMDESK

[8]   Manente G, Rech S, Lazzaretto A. Optimum choice and placement of concentrating solar power technologies in integrated solar combined cycle systems. Renewable Energy 2016;96:172–89. doi:10.1016/j.renene.2016.04.066.

[9]   Combined   Cycle   -   THERMOFLEX   (Thermoflow)   n.d. https://www.thermoflow.com/combinedcycle_TFX.html (accessed 7 April 2017).

[10]   Willnow K., 2013. Energy Efficiency Technologies ANNEX III Technical report. Energy Efficient Solutions for Thermal Power Plants. World Energy Council.

[11]   http://sel.me.wisc.edu/trnsys/(accessed 20December 2017).

[12]   Schwarzbözl, P.2006. A TRNSYS Model Library for Solar Thermal Electric Components (STEC). Reference Manual. Deutsches Zentrum für Luft and Raumfahrt.